



Cite this: DOI: 10.1039/d0ee02714f

# Recent advances and perspectives on thin electrolytes for high-energy-density solid-state lithium batteries†

Xiaofei Yang,‡ Keegan R. Adair,‡ Xuejie Gao and Xueliang Sun \*

Solid-state lithium batteries (SSLBs) are promising next-generation energy storage devices due to their potential for high energy density and improved safety. The properties and physical parameters of the solid-state electrolyte (SSE), as a critical component of the battery, have a significant effect on the electrochemical performance and energy density. In recent years, thick SSEs have been widely used in SSLBs but present several drawbacks in terms of increased internal resistance, additional inactive material content, low practical energy densities, and higher battery manufacturing costs. Reducing the thickness of SSEs and developing high-performance thin SSE-based SSLBs are essential for the commercialization of SSLBs. In this review, we comprehensively summarize the fabrication methods of thin SSEs, their rational design, and their manufacturing processes and applications in different SSLB systems. Moreover, advanced characterization techniques for understanding the Li<sup>+</sup> transport kinetics and structural evolution of SSEs at the interface are introduced. Additionally, the gravimetric/volumetric energy densities for various SSLB pouch cells with SSEs less than 100 μm thick are evaluated. Lastly, other cell design parameters are tuned to achieve gravimetric/volumetric energy densities over 300 W h kg<sup>-1</sup>/500 W h L<sup>-1</sup>, and the future directions of thin SSEs in SSLBs are speculated upon.

Received 24th August 2020,  
Accepted 2nd December 2020

DOI: 10.1039/d0ee02714f

rsc.li/ees

## Broader context

Solid-state lithium batteries (SSLBs) have been regarded as one of the most promising alternatives to state-of-the-art lithium-ion batteries due to their advantages in terms of improved energy density and safety. In the last few decades, tremendous efforts have been devoted towards exploring new solid-state electrolytes (SSEs) with high ionic conductivity and good compatibility with electrodes. Nevertheless, the thick electrolytes used in most studies result in large interfacial resistance, limited energy/power density and high battery manufacturing costs that can significantly slow down their industrialization. Thus, it is urgently required to develop thin SSEs and understand the important role they played in the electrochemical performance of SSLBs. In this review, we provide a comprehensive summary of the fabrication methods of thin SSEs and their rational design, compatibility with electrodes, and advanced characterization techniques to study the Li<sup>+</sup> transport kinetics and interface evolution at the SSE/electrode interface. Moreover, the effect of SSE thickness on energy density at the cell level was assessed and perspectives towards high-energy-density SSLBs based on thin SSEs are offered.

## 1. Introduction

In the last few decades, lithium-ion batteries have dominated the energy storage market for applications such as portable electronic devices due to their high energy/power density.<sup>1–3</sup> However, the use of liquid electrolytes has limited the potential for Li metal anodes and has hindered further improvements in energy density. To pursue next-generation energy storage

devices with higher energy density and improved safety, liquid electrolytes must be replaced with thin solid-state electrolytes (SSEs).<sup>4–7</sup> Recently, several types of SSEs have been developed, including solid polymer electrolytes (SPEs), and oxide-based, sulfide-based, and halide-based SSE systems.<sup>8</sup> Significant efforts have been devoted towards developing new SSEs and improving their ionic conductivities based on a good understanding of the Li<sup>+</sup> transport mechanisms. For instance, polyethylene oxide (PEO) is one of the most widely used SPEs, and the Li<sup>+</sup> transport along the polymer chain from one coordination site to another is associated with the breakage/formation of Li–O bonds. The long-range Li<sup>+</sup> transport is realized by local relaxation and continuous segmentation rearrangement of the

Department of Mechanical and Materials Engineering, University of Western Ontario, 1151 Richmond St, London, Ontario, N6A 3K7, Canada. E-mail: xsun9@uwo.ca

† Electronic supplementary information (ESI) available. See DOI: 10.1039/d0ee02714f

‡ These authors contributed equally to this work.

polymer chains.<sup>9</sup> The widely accepted concept is that the  $\text{Li}^+$  transport mainly occurs within the amorphous area, while the crystalline phase will hinder  $\text{Li}^+$  transport. Thus, strategies including incorporation of inorganic fillers, use of organic plasticizers, and salt design have been focused on reducing the crystallinity of PEO to achieve higher ionic conductivity.<sup>10</sup> For ceramic SSEs, the ionic conductivity is highly dependent on the concentrations of both  $\text{Li}^+$  and vacancies. Use of Li-rich materials and elemental doping to create more vacancies are two effective strategies to improve the ionic conductivity. For instance, the introduction of Li into the A site of perovskite type  $\text{ABO}_3$  (A = La, Sr, or Ca; B = Al or Ti) can create a perovskite type SSE and  $\text{Li}_{0.34}\text{La}_{0.56}\text{TiO}_3$  (LLTO), as a representative, achieved a high ionic conductivity of over  $10^{-3} \text{ S cm}^{-1}$  at room temperature (RT). Another example is  $\text{Li}_7\text{La}_3\text{Zr}_2\text{O}_{12}$  (LLZO), which is a garnet-type Li-rich material. The intrinsic ionic

conductivity is  $3 \times 10^{-4} \text{ S cm}^{-1}$  at RT, which can be further improved to  $10^{-3} \text{ S cm}^{-1}$  with a small amount of  $\text{Al}^{3+}$ ,  $\text{Ta}^{5+}$ ,  $\text{Te}^{6+}$ ,  $\text{Ga}^{3+}$ , or  $\text{Sc}^{3+}$  doping.<sup>11</sup> Alternatively, the development of new crystalline structures with fast  $\text{Li}^+$  transport channels is another strategy to improve the ionic conductivity. For instance, a one-dimensional (1D) lithium conduction pathway exists in the three-dimensional (3D) structure of  $\text{Li}_{10}\text{GePS}_{12}$  (LGPS), enabling fast  $\text{Li}^+$  diffusion and endowing it with a high ionic conductivity of over  $10^{-2} \text{ S cm}^{-1}$ .<sup>12</sup> Kanno's group found that building 3D conduction pathways based on LGPS-type crystal structure can further improve the ionic conductivity. The as-prepared  $\text{Li}_{9.54}\text{Si}_{1.74}\text{P}_{1.44}\text{S}_{11.7}\text{Cl}_{0.3}$  demonstrated an ultra-high ionic conductivity of  $2.5 \times 10^{-2} \text{ S cm}^{-1}$ .<sup>13</sup> Moreover, halide electrolytes, as a new class of SSEs with high oxidation potentials and air-stability, have received great interest.<sup>14-17</sup> Recent results have shown that the  $\text{Li}^+$  migration rate in a



**Xiaofei Yang**

*Dr Xiaofei Yang is currently a postdoctoral associate in Prof. Xueliang (Andy) Sun's Nanomaterials and Energy Group. He received his BE degree in Chemical Engineering from Anhui University, China, in 2013 and his PhD degree from the Dalian Institute of Chemical Physics, Chinese Academy of Sciences, China, in 2018 under the supervision of Prof. Huamin Zhang. His research interests focus on Li-S batteries, all-solid-state Li-ion and Li-S batteries and battery interface studies via synchrotron X-ray characterization.*



**Keegan R. Adair**

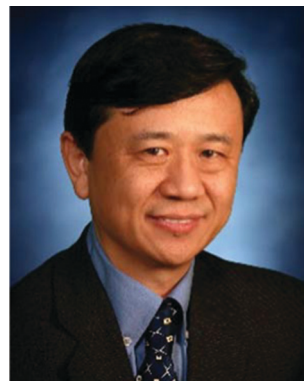
*Keegan R. Adair received his BSc in chemistry from the University of British Columbia in 2016. He is currently a PhD candidate in Prof. Xueliang (Andy) Sun's Nanomaterials and Energy Group at the University of Western Ontario, Canada. He has previous experience in the battery industry through internships at companies including E-One Moli Energy and General Motors R&D. His research interests include the design of nanomaterials for lithium metal batteries and nanoscale interfacial coatings for battery applications.*



**Xuejie Gao**

*Prof. T. K. Sham from Chemistry Department in the University of Western Ontario. Part of her work is related to the study of energy materials via synchrotron radiation.*

*Xuejie Gao is currently a PhD candidate in Prof. Xueliang (Andy) Sun's group at the University of Western Ontario, Canada. She received her BS degree in Chemistry in 2014 from Ludong University and obtained her MS degree in Chemistry in 2017 from Soochow University. Currently, her research interests focus on the development of 3D printing applied for lithium batteries. She is also co-supervised by*



**Xueliang Sun**

*University of British Columbia, Canada, and as a Research Associate at L'Institut National de la Recherche Scientifique (INRS), Canada. His current research interests are focused on advanced materials for electrochemical energy storage and conversion.*

*Prof. Xueliang (Andy) Sun is a Canada Research Chair in the Development of Nanomaterials for Clean Energy, Fellow of the Royal Society of Canada and the Canadian Academy of Engineering and Full Professor at the University of Western Ontario, Canada. Dr Sun received his PhD in materials chemistry in 1999 from the University of Manchester, UK, which he followed up by working as a postdoctoral fellow at the*

cubic-closed-packed (ccp) anion sublattice is much faster than that of a hexagonal-closed-packed (hcp) anion sublattice. Creating ccp structures *via* anion and cation radius adjustment has demonstrated to be effective in achieving high RT ionic conductivities of over  $10^{-3}$  S cm $^{-1}$ .<sup>18,19</sup> The enhanced ionic conductivity and unique properties of various SSEs have given rise to several distinct advantages. For instance, several sulfide superionic conductors possess extremely high ionic conductivities of over  $10^{-2}$  S cm $^{-1}$  at RT (*e.g.*, Li<sub>9.54</sub>Si<sub>1.74</sub>P<sub>1.44</sub>S<sub>11.7</sub>Cl<sub>0.3</sub>,  $2.5 \times 10^{-2}$  S cm $^{-1}$ ; LGPS,  $1.2 \times 10^{-2}$  S cm $^{-1}$ ), which are comparable to liquid electrolytes.<sup>12,13</sup> Other SSEs such as the halide-based Li<sub>3</sub>InCl<sub>6</sub> electrolyte have demonstrated scalable production methods, high ionic conductivity, improved air-stability and electrochemical stability up to 4.2 V.<sup>14,20</sup> Moreover, oxide-based SSEs such as Li<sub>1+x</sub>Al<sub>x</sub>Ti<sub>2-x</sub>(PO<sub>4</sub>)<sub>3</sub> (LATP), Li<sub>1+x</sub>Al<sub>x</sub>Ge<sub>2-x</sub>(PO<sub>4</sub>)<sub>3</sub> (LAGP), and LLZO exhibit excellent properties in terms of oxidation stability and thermal stability, while solid polymer electrolytes (SPEs) are associated with lower processing costs and better device integration.<sup>10</sup>

More recently, solid-state lithium batteries (SSLBs), which utilize solid-state electrolytes, have become one of the hottest areas of research for next-generation energy storage. The feasibility and safety of SSLBs assembled with Li anodes have been successfully proved in Li-LiFePO<sub>4</sub> (LFP), Li-LiCoO<sub>2</sub> (LCO), LiNi<sub>1-x</sub>M<sub>y</sub>Co<sub>1-x-y</sub>O<sub>2</sub> (NMC), Li-S and Li-O<sub>2</sub> battery systems.<sup>4,8,21,22</sup> Moreover, important battery evaluation indicators such as long cycling lives and high C-rates have also been achieved.<sup>23,24</sup> SSLBs may also prove to be more effective than their liquid counterparts, as exemplified by the cycling performance of solid-state Li-S batteries (SSLBs) where their cycle lives can be expected to be longer than those of liquid electrolyte systems due to the absence of shuttling effects.<sup>25,26</sup> It seems that the transition from batteries with liquid electrolytes to solid electrolyte systems is no longer far away. However, the development of high-energy-density SSLBs still remains challenging. The thickness of the SSEs used in many studies, especially for ceramics, has surpassed over 500 μm and

can't meet the requirements for practical application.<sup>17,27,28</sup> In order to clearly understand the effect of electrolyte thickness on energy density, we simulated the practical energy density of SSLB pouch cells based on the method proposed by Li's group and detailed information can be seen in Section 2.5.<sup>29</sup> LGPS and Li-rich (discharge capacity: 300 mA h g $^{-1}$ , discharge voltage: 4.0 V) are chosen as the representative SSE and active material, respectively. The active material content in the cathode is controlled to be 90 wt% and the negative electrode (Li) capacity/positive electrode capacity (N/P) ratio is fixed at 2. The cathode areal capacity is set as 4 mA h cm $^{-2}$ .<sup>30</sup> As can be seen from Fig. 1A and B, when the SSE thickness is 500 μm, the cathode composite (including inactive materials in the cathode) content is only 15 wt%, while the inactive SSE is as high as 77 wt%. The low active material proportion results in a low energy density of  $\sim 100$  W h kg $^{-1}$ . Upon further reducing the thickness of SSE to 100 μm, the proportion of the cathode material is increased to 39 wt% and the energy density increases to  $\sim 300$  W h kg $^{-1}$ . If the thickness of SSE can be brought down to 30 μm, a relatively high cathode material content of 54 wt% can be achieved. Under this condition, a high energy density of  $\sim 460$  W h kg $^{-1}$  is expected to be obtained, which is able to supply power for EVs up to over 500 km driving distance. In this regard, the fabrication of thin SSEs is of significance for promoting the development of high-energy-density SSLBs.

Compared with thick SSE-based SSLBs, thin SSE-based SSLBs have several merits. Firstly, reducing the thickness of SSEs can improve the gravimetric/volumetric energy density due to the decreased weight/thickness of the pouch cells. Moreover, the thickness of the SSE layer affects the internal resistance, and thus a thin SSE is beneficial for enhancing the rate performance and power density. Additionally, reducing the thickness of SSEs can reduce the cost of SSLBs, which is of significance for promoting commercialization. In addition, the structural design of SSEs to match the anode and cathode materials is equally important. The undesirable electrochemical stability window (ESW) is a common problem faced by SSEs.

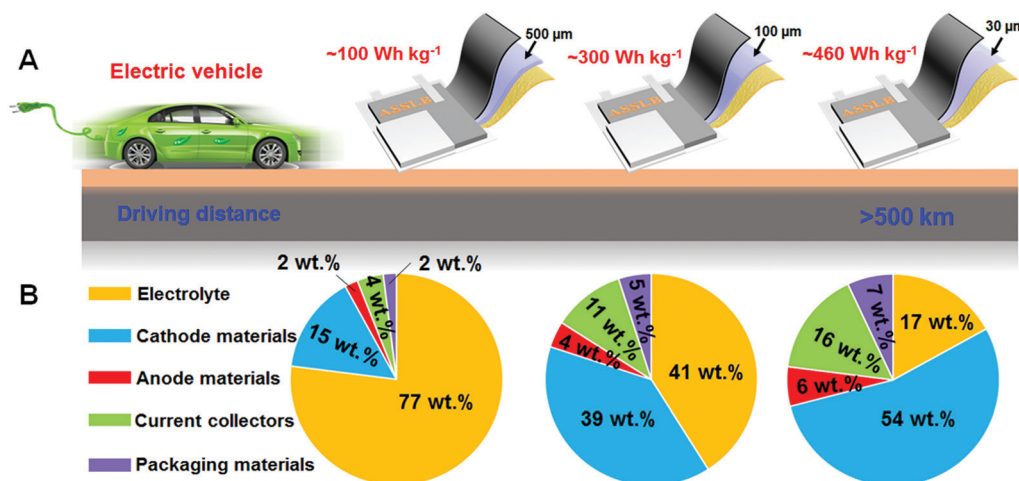


**Fig. 1** (A) The effect of electrolyte thickness on the energy density and driving distance for electric vehicles on one charge. (B) The relative weight fractions of SSLB components with electrolyte thicknesses from 500 μm down to 30 μm. The electrolyte and cathode material used here are LGPS and Li-rich, respectively.

For instance, SPEs (typically PEO electrolyte) and sulfide SSEs show oxidation stability potentials of around 4 V and less than 2.5 V, respectively, which hinders their application in high-voltage SSLBs and limits the improvement of energy density. On the other hand, high-valence metal-ion-containing SSEs (e.g.  $\text{Li}_3\text{InCl}_6$ , LGPS) display poor stability to Li anodes. The mixed ionically–electronically conductive interface promotes continuous SSE decomposition and results in increasing interfacial resistance. Moreover, the interfacial issues and Li dendrite formation related to solid–solid contact and grain boundaries also need to be taken into consideration during SSE design. In this review paper, we will summarize recent progress in the fabrication of SSEs and their application in SSLBs. Firstly, different methods for the fabrication of thin film SSEs and their manufacturing process in SSLBs will be summarized. Then, the rational design of thin SSEs and their application in different SSLB systems such as Li-ion, Li–S and Li– $\text{O}_2$  batteries will be introduced. Subsequently, advanced characterization techniques for understanding the  $\text{Li}^+$  transport rules in SSEs, the structure/composition evolution of SSEs at the interface and their response to ionic conductivity and battery performance are clarified. Then, the gravimetric/volumetric energy densities of SSLB pouch cells with SSEs with thicknesses less than 100  $\mu\text{m}$  will be evaluated. Lastly, the combination of other key parameters with thin SSEs to achieve the target of practical gravimetric/volumetric energy densities over 300  $\text{W h kg}^{-1}/500 \text{ W h L}^{-1}$  will be clarified and the future directions of thin SSEs in SSLBs will be speculated upon.

## 2. Recent progress of thin solid-state electrolytes in solid-state lithium batteries

### 2.1 Fabrication of thin solid-state electrolytes

As aforementioned, the development of thin SSEs is of significance to ensure high energy density/power density output for SSLBs. However, before understanding the challenges in realizing thin SSEs, we must first introduce their common fabrication methods. All the fabrication methods mentioned here are aimed towards bulk SSLBs with high-energy-density and the popular methods for nano-scale layer fabrication (e.g. physical vapor deposition, atomic layer deposition) for thin-film SSLBs are not included. Fig. 2 illustrates seven common methods including solution/slurry casting, tape casting, solution infusion, hot/cold pressing, extrusion, 3D printing and other methods. Each method will be discussed in detail in the following sections. A summary of thin SSEs with thicknesses of no more than 100  $\mu\text{m}$  based on the aforementioned fabrication methods and their applications is provided in Table S1 (ESI<sup>†</sup>).

**2.1.1 Solution/slurry casting.** Among the various fabrication methods, solution/slurry casting has been widely adopted and has been regarded as an available and scalable method for practical application. Solution casting is suitable for the preparation of SPEs and polymer-containing composite electrolytes,<sup>31,32</sup> while the slurry casting method is suitable

for the fabrication of ceramic SSEs with binders that can interconnect the SSE particles. Generally, there are two types of products obtained by the solution/slurry casting method: (1) free-standing SSEs and (2) cathode-supported SSEs. The former is realized by simply pouring the solution/slurry into an inert mold or by blade casting on an inert substrate, and then evaporating the solvents. The thickness can be controlled by adjusting the volume and concentration of the solution/slurry. For instance, Yang's group and Wei's group successfully obtained 70  $\mu\text{m}$  and 80  $\mu\text{m}$  PEO-based hybrid SPEs *via* a solution casting method and applied them in Li–S batteries and Li–LFP batteries.<sup>33,34</sup> In another case, Lee *et al.* fabricated a 40  $\mu\text{m}$   $\text{Li}_6\text{PS}_5\text{Cl}$  SSE based on a slurry casting method.<sup>23</sup> The cathode-supported SSE can be achieved by casting the slurry directly on the surface of the cathode. For the free-standing SSE, a layer with a relatively high thickness of over 30  $\mu\text{m}$  is necessary to ensure sufficient mechanical integrity when detaching the solidified SSE from the mold or substrate. For the cathode-supported SSE, the thickness can be further reduced to 5–10  $\mu\text{m}$ . Wang and co-workers repeated the solution casting process on a cathode and achieved an ultrathin cathode-supported SSE film (Fig. 2A). The SSE film was determined to be 9.5  $\mu\text{m}$  according to the scanning electronic microscopy (SEM) images. In another study, an ultrathin LLZO SSE layer with a thickness of 5  $\mu\text{m}$  was realized *via* this method.<sup>35</sup> Moreover, the cathode/SSE interfacial resistance is further reduced, thus enabling better electrochemical performance.<sup>36</sup>

Solvents, as an important component of the fabrication process, should be carefully chosen during solution/slurry casting. An ideal solvent should have a low boiling point in order to be easily removed after the casting process. Moreover, it should be chemically inert towards the material being dispersed and have good solubility for polymers and Li salts. For instance, in the widely used poly(ethylene oxide) (PEO) system, acetonitrile is the most commonly used solvent due to its ability to dissolve PEO and chemical inertness towards inorganic fillers such as LLZO and  $\text{SiO}_2$ .<sup>10</sup> In the sulfide SSE system, non-polar solvents such as xylene and *n*-hexane are chosen as the common solvents.<sup>23,37</sup> Moreover, the selection of binders and their content in the electrolyte is another consideration. Conventional binders such as polyvinylidene fluoride (PVDF) and carboxymethyl cellulose (CMC) are extruded due to their poor solubility in non-polar solvents. Rubbers such as styrene–butadiene rubber (SBR) and silicon rubber (SR) have been widely adopted as the binders with xylene as the solvent for the fabrication of sulfide SSEs.<sup>37</sup> Additionally, the ionic conductivity of SSEs will be affected by non-conductive binders to some extent, thus resulting in increased impedance in SSLBs. With this in mind, it is necessary to control the binder content by balancing the ionic conductivity and adhesion strength.

**2.1.2 Tape casting.** Tape casting, also known as doctor blading or knife coating, has been widely used to produce large, thin ceramic layers (Fig. 2B).<sup>38</sup> Firstly, the ceramic SSE powders along with an organic binder should be dispersed or dissolved into a solvent. Subsequently, the homogenous slurry is loaded into the flexible substrate through the use of an

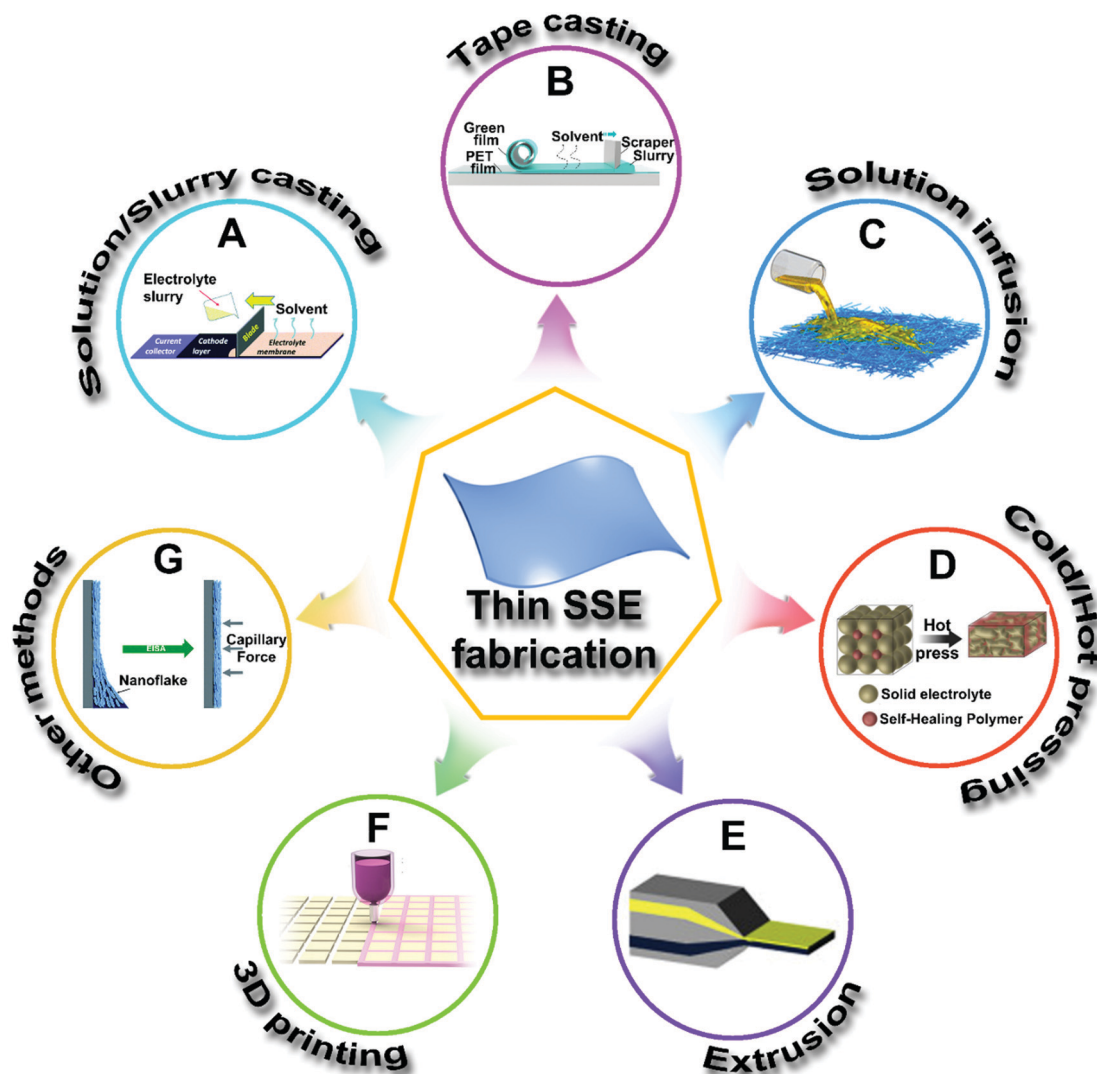


Fig. 2 Fabrication methods for thin SSEs. (A) Solution/slurry casting method. Reproduced with permission from ref. 36. Copyright (2019) Royal Society of Chemistry. (B) Tape casting method. Reproduced with permission from ref. 41. Copyright (2020) Wiley-VCH. (C) Solution infusion method. Reproduced with permission from ref. 50. Copyright (2020) American Chemical Society. (D) Cold/hot pressing method. Reproduced with permission from ref. 55. Copyright (2015) Wiley-VCH. (E) Extrusion method. Reproduced with permission from ref. 58. Copyright (2018) Elsevier. (F) 3D printing method. Reproduced with permission from ref. 59. Copyright (2019) American Chemical Society. (G) Other methods. Reproduced with permission from ref. 60. Copyright (2016) Royal Society of Chemistry.

adjustable doctor-blade. Followed by evaporation of the solvent, flexible ceramic films with thicknesses in the range of 20–1000  $\mu\text{m}$  are obtained. To further improve the interconnectivity of the ceramic particles, a hot press process is typically used to reduce the interfacial resistance after solvent evaporation. During the annealing process, the organic components are evaporated whereupon a thin and dense ceramic SSE film is obtained.<sup>38–43</sup> For instance, Wang and his co-workers reported a series of thin LLTO SSEs with thicknesses in the range of 25–160  $\mu\text{m}$ .<sup>41</sup>

One advantage of the tape casting technique is that it is not limited to the preparation of single-layer ceramic SSEs. Simply repeating the casting steps or laminating single-layer tapes can lead to multi-layered ceramic SSEs with different functionalities. Hu's and Wachsman's groups have successfully realized

bi-layered and tri-layered  $\text{Li}_7\text{La}_{2.75}\text{Ca}_{0.25}\text{Zr}_{1.75}\text{Nb}_{0.25}\text{O}_{12}$  (LLCZNO) and LLZO SSEs.<sup>44–46</sup> With the introduction of poly(methyl methacrylate) (PMMA) into the top and bottom layers, which acted as the pore forming agent, porous SSE layers with controllable pore distribution were achieved. Thus, an electrolyte layer with a porous–dense–porous structure was obtained. The dense middle layer acts as the primary SSE layer, while the top and bottom porous layers act as hosts for Li and active materials.<sup>45,46</sup> According to their results, the thicknesses of the dense layer and porous layer are  $\sim 15 \mu\text{m}$  and 50–70  $\mu\text{m}$ , respectively.

**2.1.3 Solution infusion.** Solution infusion is another method for thin SSE fabrication, which is based on the infusion of a SSE-containing slurry or solution into a porous substrate.<sup>47–52</sup> After removing the solvent or inactive organic components, a thin SSE film is achieved. Generally, the thickness of the as-prepared

SSE film is determined by the porous substrate, while the ionic conductivity is greatly affected by the SSE and the substrate. Recently, this method has been successfully applied in the preparation of both SPEs and ceramic SSEs. For SPE fabrication, an ideal substrate is an interconnected inorganic ionic conductor, which can provide continuous channels for SPE infusion. On one hand, the SPE improves the flexibility of the composite, while the inorganic component enhances the mechanical strength. On the other hand, the continuous inorganic and SPE ion transport pathways are necessary to achieve high ionic conductivity. Yu's group designed a three-dimensional (3D) nanostructured hydrogel-derived LLTO host for polymer infusion and achieved a high RT ionic conductivity of  $8.8 \times 10^{-5} \text{ S cm}^{-1}$ . In another study, Hu and his coworkers developed a thin interconnected 3D LLZO host *via* an electrospinning method for SPE infusion. The as-prepared hybrid SSE possessed a high RT ionic conductivity of  $2.5 \times 10^{-4} \text{ S cm}^{-1}$  with a thickness of 40–50  $\mu\text{m}$ .<sup>47</sup>

For thin film ceramic SSE fabrication, finding a suitable solvent for dissolving ceramic SSEs is important. Moreover, the substrate should be chemically inert to the solvent and SSE at RT or annealing temperatures. Moreover, in order to reduce the effect of the substrate (if it is a non-ionic conductor) on the ionic conductivity, the substrate should have significant porosity. More importantly, the substrate should have a high thermal tolerance and maintain its flexibility under the annealing conditions. By taking all the features into consideration, Jung's group fabricated a sulfide SSE based on the solution infusion method. Firstly, they dissolved the  $\text{Li}_6\text{PS}_5\text{Cl}_{0.5}\text{Br}_{0.5}$  SSE into an ethanol solvent (Fig. 2C). Subsequently, they infused the solution into electrospun polyimide (PI) nonwovens, where the PI can tolerate a high temperature of 400 °C, which was used during the SSE annealing process. Afterwards, 40–70  $\mu\text{m}$   $\text{Li}_6\text{PS}_5\text{Cl}_{0.5}\text{Br}_{0.5}$  SSEs with a high ionic conductivity of  $2.5 \times 10^{-3} \text{ S cm}^{-1}$  were achieved.<sup>50</sup>

**2.1.4 Cold/hot pressing.** Cold/hot pressing is another popular method for thin SSE fabrication. Cold pressing is a simple method that mechanically presses SSEs (typically a soft sulfide SSE) into a porous host at RT.<sup>53,54</sup> However, it is difficult to achieve uniform distribution of the SSE particles throughout the host with this method. Generally, a solvent-assisted dispersion process is required to ensure a uniform thin sulfide SSE film. In most cases, non-polar solvents such as toluene and heptane are chosen to prevent the structural change because of side reaction between SSEs and solvents. For instance, Jung's group cold-pressed  $\text{Li}_3\text{PS}_4$  and LGPS into nonwoven scaffolds and achieved sulfide SSEs with high ionic conductivities of  $7.3 \times 10^{-4} \text{ S cm}^{-1}$  and  $4 \times 10^{-3} \text{ S cm}^{-1}$ , respectively.<sup>53</sup> The thickness of the SSEs was determined to be 70  $\mu\text{m}$ . A similar process was reported by Wang's group, where the cathode-supported SSE was around 100  $\mu\text{m}$ .<sup>54</sup>

In contrast, hot pressing is a heat-assisted process, which is applied in SPE and binder-containing ceramic SSE fabrication (Fig. 2D). The applied heat can melt the polymers or binders and eliminate the use of solvents. Before the hot press process, thorough mixing of the polymers/Li salts and ceramic SSEs/binders is required to form a homogeneous mixture. For ceramic

SSE fabrication, the introduction of a binder can enhance the flexibility of the SSE, which is of significance in large-scale production. Nevertheless, the addition of a binder will reduce the ionic conductivity of the SSE after hot pressing. Hence, for practical applications, the binder content in the SSEs should be minimized to balance the ionic conductivity and flexibility. Recently, both free-standing SPEs and ceramic SSEs with thicknesses less than 100  $\mu\text{m}$  have been successfully fabricated by the hot pressing method, proving it is a promising method for thin SSE preparation.<sup>55–57</sup>

**2.1.5 Extrusion.** The extrusion process is another scalable method to fabricate thin SSEs from high-viscosity mixtures.<sup>58,61</sup> Before the extrusion process, it is necessary to obtain a homogeneous viscous paste by mixing the polymers/Li salts or binder/ceramic SSEs at elevated temperatures in a mixing chamber. Subsequently, the electrolyte slurry is fed through a flow channel and the electrolyte slurry is extruded into a thin electrolyte sheet. With this process, Passerini's group developed a hybrid  $\text{LLZO-P(EO)}_{15}\text{LiTFSI}$  (LiTFSI is the abbreviation for lithium bis(trifluoromethanesulfonyl)imide) SSE with a thickness of less than 100  $\mu\text{m}$ .<sup>62</sup> In another case, the same group developed a 90  $\mu\text{m}$   $\text{PEO-LiN(SO}_2\text{CF}_2\text{CF}_3)_2$  (LiBETI) electrolyte and applied it as the SSE in a 0.6 A h  $\text{Li/V}_2\text{O}_5$  pouch cell. The pouch cell demonstrated a low capacity decay of 0.3% per cycle within 140 cycles.<sup>63</sup> During this process, small amounts of solvents could be used to process sulfide electrolyte powders, enabling the production of binder-free sulfide electrolyte layers.<sup>64</sup> Moreover, the extrusion process can also be used to fabricate cathode-supported SSEs by extruding the cathode and SSE concurrently. The process is also known as a co-extrusion process (Fig. 2E). The advantage of this process is the solvent-free processing and the formation of low porosity, flexible membranes, thus eliminating the deteriorate effect of solvents on the ionic conductivity of some SSEs. Compared with the solution/slurry casting method, a limited throughput is a disadvantage.<sup>58</sup>

**2.1.6 3D printing.** 3D-Printing has received significant attention in the field of energy storage devices due to its ability to construct 3D-structured electrodes and electrolytes with micro-scale precision.<sup>65,66</sup> Benefitting from its accuracy in printing micro-scale patterns, its application has been extended to the design of thin SSEs.<sup>59,67,68</sup> Printing a SSE slurry onto a substrate is a simple and effective fabrication strategy. The thickness of the as-prepared SSEs can be easily adjusted by controlling the concentration of SSE in the slurry and the number of layers in the printed pattern. Recently, as shown in Fig. 2F, Hu and his coworkers developed a flexible electrolyte membrane (thickness: 50–250  $\mu\text{m}$ ) with a tile-and-grout pattern *via* 3D printing, where the garnet-type electrolyte tile-like chips are joined together without gaps using styrene-butadiene copolymer. The garnet chips act as fast lithium-ion transport channels, while the polymer grid serves as a buffer to reduce the stress among the garnet chips.<sup>59</sup> In another study, Kim *et al.* developed an ultraviolet (UV) curing-assisted 3D printing method to form a thin SPE layer on the surface of a sulfur cathode. They first printed the photosensitive SPE precursors on the printed sulfur cathode and then exposed the electrode

to UV light. The precursors were polymerized on the sulfur cathode and functioned as a SPE. According to their SEM image, the thickness of the SSE is around 40  $\mu\text{m}$ .<sup>68</sup>

**2.1.7 Other methods.** Besides the aforementioned methods, some other techniques for the fabrication of thin SSEs have been reported. For instance, a hydrothermal method was utilized to grow thin LAMP SSE layers on the surface of graphite. The thicknesses of the LAMP SSE could be adjusted in the range of 40–90  $\mu\text{m}$  by controlling the hydrothermal process from 15 to 24 h.<sup>69</sup> Solvent evaporation has also proven to be an effective technique in fabricating thin SSEs with thicknesses less than 50  $\mu\text{m}$  (Fig. 2G).<sup>60,70,71</sup> Moreover, *in situ* polymerization is also a popular method to form thin film polymer SSEs between the anode and cathode.<sup>72,73</sup> This technique typically entails the assembly of an unsealed cell followed by infusion of the SPE precursors. The cell is then treated with suitable conditions to induce polymerization of the SPE precursors, which have intimate contact with other cell components. The *in situ* formed SSE can significantly reduce the interfacial resistance as well as act as an interconnected ion conducting network in the electrodes. The thickness of the SPE layer is largely determined by the gap between the cathode and anode.<sup>72</sup>

In summary, the fabrication of thin SSEs with thicknesses less than 100  $\mu\text{m}$  benefits the energy density of SSLBs. Slurry/solution casting is a promising method to fabricate scalable thin SSEs. However, the method still faces challenges in the selection of suitable solvents and binders, especially for sulfide SSE systems. Tape casting, a widely used thin oxide SSE fabrication method, has shown promise in fabricating oxide SSEs with thicknesses of less than 20  $\mu\text{m}$ , but the complicated process and limited throughput hinder its practical application to some extent. Embedding SSEs into porous hosts *via* solution infusion and cold pressing methods shows advantages such as improved mechanical strength. However, the use of non-conductive hosts will decrease the ionic conductivity. With this in mind, ionically conductive hosts or hosts with high porosity are suggested. Moreover, the solution infusion method is only compatible with a few candidate SSEs such as  $\text{LiP}_6\text{S}_5\text{Cl}$ ,  $\text{Li}_7\text{P}_3\text{S}_{11}$ , and  $\text{Li}_3\text{InCl}_6$ , which can be synthesized in solvents.<sup>14,20,74–76</sup> Additionally, in order to achieve crystal structures with high ionic conductivities, an annealing process is necessary. Thus, the host must be able to tolerate high temperatures. Polymers such as PI, polyethyleneimine (PEI), and polyethylene terephthalate (PET) are good choices.<sup>50</sup> Compared with solvent-based solution/slurry casting and solution infusion methods, the solvent-free hot pressing and extrusion methods could effectively circumvent the deteriorating effect of solvents on the ionic conductivity. For ceramic SSE fabrication, the introduction of non-conductive binders will reduce the ionic conductivity. Hence, for practical application, it is suggested that non-conductive binders are replaced with ionically conductive alternatives or minimize the binder content. Additionally, other methods such as 3D printing, solvent-thermal, and *in situ* polymerization methods show promise in specialized systems. We believe that it is still of significance to develop more thin SSE fabrication methods

by taking scalability, cost, ionic conductivity, and thickness into consideration.

## 2.2 Manufacturing of lithium batteries with thin solid-state electrolytes

The manufacturing process for thin SSEs and their integration in SSLBs, especially for practical pouch cells, are critical to their commercialization. With this in mind, before talking about the application of thin SSEs in different SSLB systems, the manufacturing and assembly processes of full cells based on the fabrication methods mentioned in Section 2.1 will be discussed below.

**2.2.1 Stacking manufacturing process.** The stacking manufacturing process is one of the most popular methods for SSLBs and is similar to that of state-of-the-art Li-ion batteries. As illustrated in Fig. 3A, the cell assembly can be easily realized by stacking of the cathode, electrolyte, and anode layers. Generally speaking, this manufacturing process is suitable for the aforementioned free-standing thin SSEs obtained in Section 2.1. However, the interfacial issues associated with prefabrication of individual layers and subsequent stacking may be problematic. For SPEs, the interfacial resistance between electrode and electrolyte can be relieved by a heating process, where semi-melted SPEs can wet both anode/electrolyte and cathode/electrolyte interfaces. For soft sulfide SSEs, a pressing process is needed to improve the mechanical contact between electrolyte and electrodes. For rigid oxide SSEs, a small amount of liquid electrolyte, ionic liquid, or SPE should be introduced into the electrolyte/electrode interfaces to reduce the interfacial resistance.

**2.2.2 Slurry cast manufacturing process.** As mentioned in Section 2.1.1, the thin SSEs obtained by the solution/slurry casting method can be classified into two categories: free-standing SSEs and cathode-supported SSEs. Free-standing SSEs can be used to assemble SSLBs with the stacking manufacturing method, while cathode-supported SSEs are more suitable for the slurry casting manufacturing process. As illustrated in Fig. 3B, automated manufacturing is expected to be applied for large-scale SSLB fabrication.<sup>77</sup> Firstly, a slurry casting method is used to fabricate the cathode. Subsequently, another SPE or sulfide SSE layer will be cast on the dried cathode surface. In this process, homogeneous electrode/electrolyte distribution and suitable binders/solvents are crucial factors that will inevitably affect the ASSB performance. After casting of the electrolyte on the cathode surface, a Li anode layer will be calendered on the cathode-supported SSEs. In the final stage of the assembly process, the tri-layered cathode–SSE–anode structure will be cut using a laser in preparation for stacking and packaging. Compared with the stacking manufacturing process in Section 2.2.1, wet manufacturing can significantly reduce the interfacial resistance. However, this method is still not suitable for oxide SSE-based SSLBs due to their intrinsically large contact resistance. Nevertheless, this manufacturing process can be extended to quasi-SSLBs with the introduction of small amounts of liquid electrolytes or ionic liquids to accelerate  $\text{Li}^+$  transport between the oxide SSE powders.

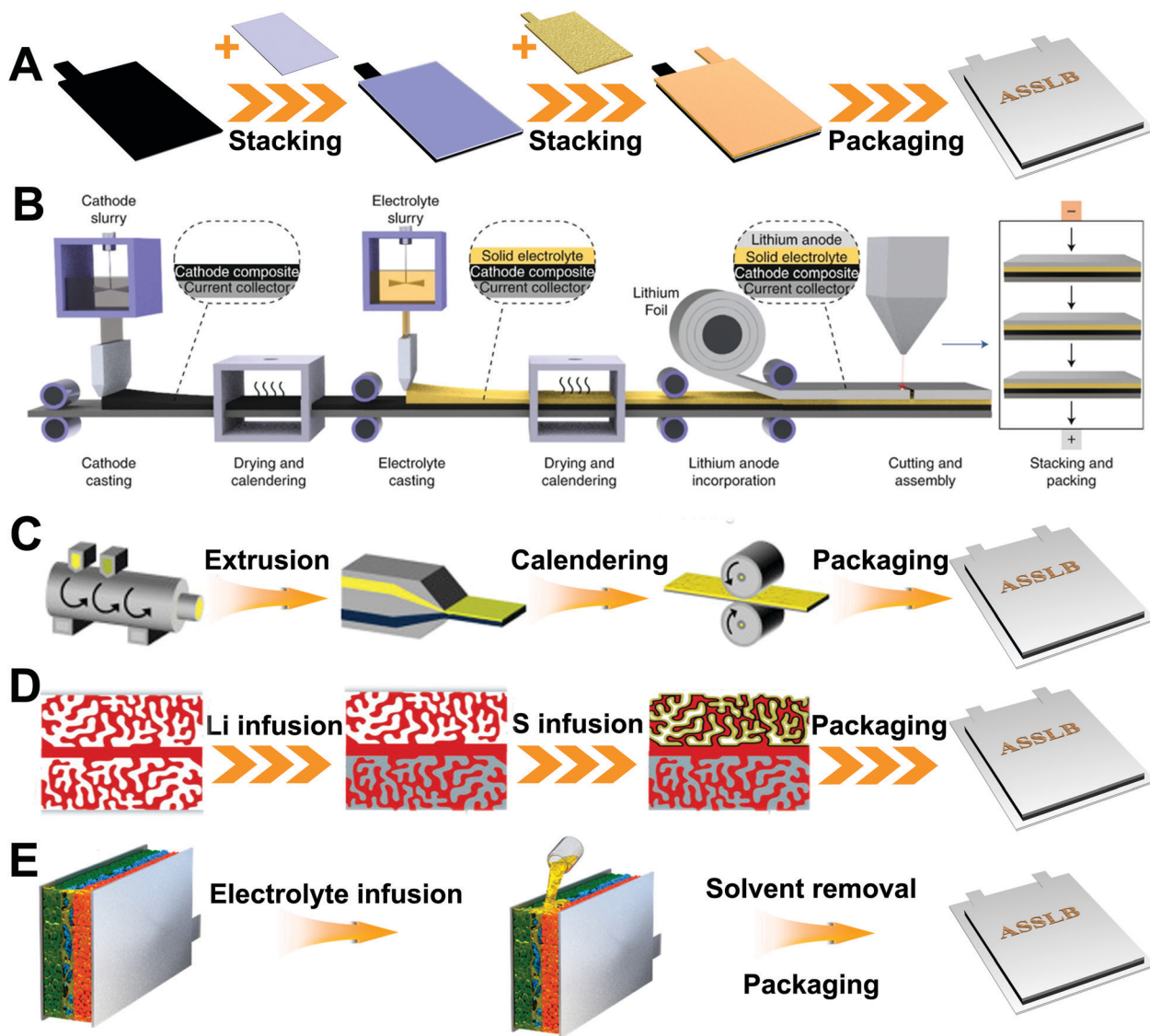


Fig. 3 Manufacturing of lithium batteries based on thin solid-state electrolytes. (A) Stacking manufacturing process. (B) Slurry/solution casting manufacturing process. Reproduced with permission from ref. 77. Copyright (2020) Nature Publishing Group. (C) Extruding manufacturing process. Reproduced with permission from ref. 58. Copyright (2018) Elsevier. (D) Tape casting manufacturing process. Reproduced with permission from ref. 45. Copyright (2018) Elsevier. (E) Electrolyte infusion manufacturing process. Reproduced with permission from ref. 50. Copyright (2020) American Chemical Society.

**2.2.3 Extrusion manufacturing process.** The extrusion manufacturing process is another method of engineering SSLBs that is suitable for high-viscosity systems.<sup>58</sup> As mentioned in Section 2.1.5, the co-extrusion process can be applied to fabricate cathode-supported SSEs, which is very similar to the slurry/solution casting process. Upon further pressing or calendaring a Li anode layer on the surface, a trilayer cathode-SSE-anode structure can be achieved, which can be further cut into small units for stacking and packaging (Fig. 3C). This manufacturing process can be automated and has been adopted by Palo Alto Research Center (PARC) and Bathium Canada Inc.<sup>78,79</sup> PARC has demonstrated a high capacity of over  $120 \text{ mA h g}^{-1}$  at C/3 with a thick electrode of  $62.5 \mu\text{m}$  within polymer electrolyte.<sup>79</sup>

**2.2.4 Tape casting manufacturing process.** Section 2.1.2 has shown that tape casting can be used to fabricate bi-layer porous-dense and tri-layer porous-dense-porous structures.<sup>44-46</sup> In the former case, a cathode-SSE-anode unit can be assembled by introducing Li foil on the surface of the dense SSE layer, while the porous structure is used for cathode material infusion (soluble active materials such as sulfur). For insoluble active materials such as LCO and  $\text{V}_2\text{O}_5$ , it is more practical to sinter the cathode with electrolyte during the annealing process.<sup>80,81</sup> To reduce the interfacial resistance between the electrolyte and SSE, small amounts of liquid electrolytes should be added. Compared with the bi-layer structure, the tri-layer structure can further reduce the interfacial resistance of the anode/electrolyte side by infusing molten Li into the porous structure (Fig. 3D).

Afterwards, a SSLB pouch cell can be obtained by packaging the cathode–SSE–anode units. This technique is among the most popular methods for fabricating oxide-based SSLBs. However, compared with slurry casting and extrusion manufacturing, the tape casting manufacturing process is more complicated and has limited throughput potential.

**2.2.5 Electrolyte infusion manufacturing process.** The electrolyte infusion manufacturing process is similar to the injection process in liquid electrolyte batteries. Firstly, the cathode, anode and separator (works as the electrolyte host) are stacked and then stored in a package with one side unsealed. Subsequently, electrolyte solution (electrolyte dissolved into a solvent or small molecule monomers and Li salts for polymerization) is infused into the package to wet the cathode, anode and separator. For the *in situ* polymerization process, the package can be directly sealed and then treated with suitable conditions (e.g. thermal polymerization) to let the monomers polymerize into SPEs.<sup>73</sup> For solvent-containing electrolytes, it is necessary to remove the solvents before sealing the package. Generally, the electrolyte fills the pores in the cathode and separator, acting as the Li<sup>+</sup> transport channels to facilitate the Li<sup>+</sup> transport between the anode and cathode. Moreover, benefitting from the good wettability of the electrolyte solution, the interfacial resistance can be significantly reduced. During this process, several factors should be carefully taken into consideration: (1) solvents and electrolytes should be stable to electrode materials, current collectors and package materials; and (2) for ceramic electrolytes such as Li<sub>6</sub>PS<sub>5</sub>Cl and Li<sub>3</sub>InCl<sub>6</sub>, a relatively high post-treatment temperature is necessary to recover the high-ionic conductivities of the electrolytes.<sup>20,50</sup> In this regard, it is important to choose suitable electrode materials, separators, and package materials to meet the requirements of post-treatment. Another option is to sacrifice the ionic conductivity of the electrolyte by using a low post-treatment temperature to ensure the stability of electrode materials, separators and package materials. In practical application, the two choices should be balanced: (3) for ceramic electrolytes, the precipitation of electrolytes still shows high contact resistance and external pressure should be applied to ensure good Li<sup>+</sup> transport; and (4) this process is not suitable for multi-layer electrolyte systems.

In summary, battery manufacturing is a very important step towards realizing thin SSEs in SSLBs, especially for large-size pouch cells. The stacking, slurry casting and extrusion manufacturing processes show promise in engineering SPE, SPE-based hybrid SSE, and sulfide SSE-based SSLBs. More attention should be focused on solving the interfacial issues of the stacking manufacturing process due to the individually fabricated components. Post-treatment processes such as heating, pressing, and infusing liquid electrolyte/ionic liquid should be considered in different systems. Slurry casting and extrusion are automatic manufacturing processes, which can be used to continuously produce cathode–SSE–anode layers. Suitable SSE systems should be explored based on these two methods. Considering the better mechanical properties and environmental stability, SPEs and SPE-based hybrid SSEs are likely the first step

for SSLB manufacturing. Tape-casting is one of the best methods for the fabrication of thin oxide SSEs and oxide SSE-based SSLBs with high ionic conductivity. Nevertheless, its scalability and manufacturing costs are still not comparable to the aforementioned processes. In this regard, more efforts should be devoted towards exploring alternative battery manufacturing processes for oxide SSEs. The electrolyte infusion manufacturing process is a similar process to that of the injection process in liquid electrolyte systems. Nevertheless, the stability of electrode materials, separators and packaging materials to solvents and electrolytes should be carefully considered. Moreover, the contradiction of the thermal stability of the battery materials and high ionic conductivity of the electrolyte under high temperature post-treatment is another factor that should be taken into consideration. Additionally, it is still challenging to realize uniform multi-layer electrolyte distribution in battery systems based on this manufacturing process. Therefore, one suitable electrolyte system should be chosen to meet all the requirements of both the anode and cathode.

### 2.3 Application of thin solid-state electrolytes in lithium batteries

SSLBs assembled with thin SSEs and Li metal have the potential to deliver high energy densities with improved safety. In Section 2.1, we have introduced several methods for fabricating thin SSEs. However, these methods alone are not enough to achieve high-energy-density SSLBs. Rational design of SSEs with multi-structures, functions and properties to meet the various requirements of different SSLB systems is also very important. In this section, we will introduce the rational design of thin SSEs and their application in different SSLB systems. According to the different types of cell configurations, they can be classified into coin/model cells and pouch cells. In Sections 2.3.1–2.3.4, we will introduce the application of thin SSEs in coin/model cells, including Li–LFP, Li–LCO/NMC, Li–S and Li–O<sub>2</sub> batteries. In Section 2.3.5, pouch cell designs closer to practical application will be summarized.

**2.3.1 Solid-state Li–LFP batteries.** Li–LFP batteries are one of the most popular SSLB systems due to the use of nano-sized active materials which can facilitate Li<sup>+</sup>/e<sup>−</sup> transport, as well as the lower operating voltage range (typically 2.5–4.0 V) which is within the ESWs of many SSEs.<sup>48,56,72,82–86</sup> PEO, one of the most widely used SPEs, possesses considerable ionic conductivity at a working temperature of over 60 °C, high flexibility, and good interface wettability in Li–LFP SSLBs. Moreover, its high stability to Li metal and oxidation potential of 4.0 V are also desirable properties for PEO's application in Li–LFP SSLBs. If the Li metal anode is combined with a thin SSE, Li–LFP SSLBs have the potential to deliver a high energy density of over 200 W h kg<sup>−1</sup>, which has been confirmed by Huang's group.<sup>87</sup> An ultrathin PEO SPE with a thickness of 7.5 μm was developed by infusion of a PEO and Li salt solution into a commercial polyethylene separator (labeled PPL, Fig. 4A). Benefitting from the shortened Li<sup>+</sup> diffusion distance within the PPL electrolyte, the assembled Li–LFP cell showed improved rate performance. At a high rate of 10C, the Li–LFP cell assembled with the PPL

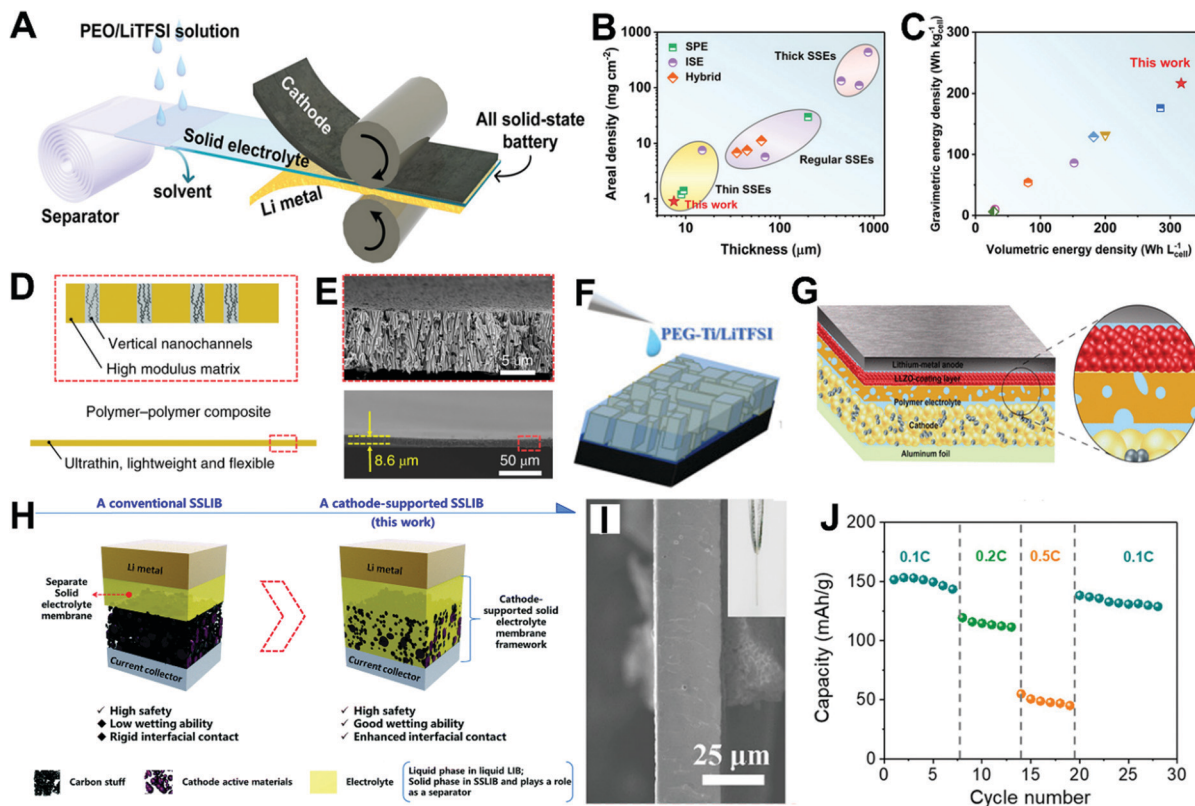


Fig. 4 (A) Schematic illustration of SSLB assembly with PPL electrolyte. (B) Comparison of the thickness and areal density of PPL electrolyte with those of previously reported SSEs. (C) Comparison of the gravimetric and volumetric energy densities of PPL SSLBs with other state-of-the-art SSLBs. Reproduced with permission from ref. 87. Copyright (2019) Wiley-VCH. (D) Schematic showing the design principles of PI-PEO SPE and (E) relevant cross-sectional SEM images of an ultrathin PI host. Reproduced with permission from ref. 48. Copyright (2019) Nature Publishing Group. (F) Schematic illustration of a Li<sub>7</sub>P<sub>3</sub>S<sub>11</sub> host for PEG-Ti SPE infusion. Reproduced with permission from ref. 86. Copyright (2019) Elsevier. (G) Schematic diagram of the LLZO/LFP interface modified with an *in situ* polymerized SPE. Reproduced with permission from ref. 72. Copyright (2018) American Chemical Society. (H) Schematic of the construction of a conventional Li-LFP SSLB and a cathode-supported Li-LFP SSLB. Reproduced with permission from ref. 36. Copyright (2019) Royal Society of Chemistry. (I) Cross-sectional SEM image of LLTO SSE fabricated by a tape casting technique. (J) Rate performance of the Li-LFP SSLB assembled with LLTO SSE at 65 °C. Reproduced with permission from ref. 41. Copyright (2020) Wiley-VCH.

electrolyte delivered a high capacity of over 50 mA h g<sup>-1</sup> at 60 °C, which is almost two times higher than its counterpart with the solution cast PEO electrolyte (120 μm) at 5C. Moreover, a high active material loading Li-LFP SSLB (LFP loading: 7.0 mg cm<sup>-2</sup>) was shown to have stable electrochemical performance for 50 cycles. More importantly, their results showed that the as-prepared thin PPL had a low areal density of less than 1 mg cm<sup>-2</sup>, which is almost 10 times lower than those of previously reported SPEs (Fig. 4B). Combined with a Li metal anode, the assembled Li-LFP cell has the potential to deliver a high gravimetric/volumetric energy density of 216 W h kg<sup>-1</sup>/317 W h L<sup>-1</sup> (excluding packaging, Fig. 4C). In order to achieve better electrochemical performance, it is critical to search for strategies which can improve the ionic conductivity of SPEs. Considering the effect of tortuosity on the Li<sup>+</sup> transport and ionic conductivity in SPEs, Cui's group developed a PI membrane with vertically-aligned channels for PEO SPE infusion (labeled PI-PEO, Fig. 4D and E). Compared with the pure PEO SPE (130 μm) obtained from blade-casting, the as-prepared PI-PEO SPE (8.6 μm) displayed a high RT-ionic conductivity of 2.3 × 10<sup>-4</sup> S cm<sup>-1</sup>, which is over 4 times higher than its counterpart

(5.4 × 10<sup>-5</sup> S cm<sup>-1</sup>).<sup>48</sup> Introducing inorganic fillers is another effective method to improve the ionic conductivity.<sup>52,82,86</sup> Lin *et al.* developed a 3D SiO<sub>2</sub>-aerogel scaffold as the PEO SPE host and the obtained SiO<sub>2</sub>-aerogel-PEO composite electrolyte exhibited a high RT ionic conductivity of 6 × 10<sup>-4</sup> S cm<sup>-1</sup>. The high ionic conductivity enabled stable cycling of the Li-LFP cells for over 200 cycles with a capacity of over 100 mA h g<sup>-1</sup> at 0.5C (LFP loading: ~1 mg cm<sup>-2</sup>). Moreover, Li-LFP SSLBs with a high LFP loading of 13.6 mg cm<sup>-2</sup> delivered a high areal capacity of 2.1 mA h cm<sup>-2</sup> (cycling life: 13 cycles, operating temperature: 55 °C). In another case, carbon quantum dots (CQDs) were introduced to improve the ionic conductivity of SPEs. The results showed that the CQDs can act as Lewis acids to increase the dissociation degree of lithium salts, the adsorption of anions and the amorphicity of the PEO matrix. As a result, the PEO/CQD electrolyte delivered a high ionic conductivity of 1.39 × 10<sup>-4</sup> S cm<sup>-1</sup> and a high lithium transference number of 0.48 at RT. Benefitting from the improved ionic conductivity, the assembled Li-LFP SSLB demonstrated excellent rate performance and improved power density. At a high rate of 8C, the SSLB using the PEO/CQD electrolyte

delivered a high capacity of  $88 \text{ mA h g}^{-1}$ , which is much higher than its counterpart using PEO electrolyte ( $13 \text{ mA h g}^{-1}$ , operating temperature:  $60 \text{ }^\circ\text{C}$ )<sup>34</sup> Compared with non-ionically-conductive inorganic fillers, inorganic SSE fillers are more promising in enhancing the ionic conductivity of thin SPEs. For instance, a thin 3D  $\text{Li}_7\text{P}_3\text{S}_{11}$  host ( $\sim 10 \text{ }\mu\text{m}$ ) was fabricated by a slurry coating method for PEG-Ti SPE infusion and achieved an improved RT ionic conductivity of  $1.6 \times 10^{-4} \text{ S cm}^{-1}$ . Benefitting from the thin SSE and high ionic conductivity, the assembled Li-LFP SSLB delivered a high discharge capacity of  $125 \text{ mA h g}^{-1}$  at RT (rate: 0.05C). A good interface also plays an important role in enhancing the battery performance. *In situ* polymerization of polymer precursors and coating the SPE solutions on a cathode have proven to be effective in developing interfaces with intimate contact due to the complete wetting of both the surface and internal particles of electrodes with the liquid precursors. In this regard, the *in situ* formed SPEs play two roles: (1) on the surfaces of the electrodes, the SPEs act as the ionically conductive separators to transport  $\text{Li}^+$  and physically separate the anode and cathode; and (2) within the electrodes, the SPEs function as ionic transport pathways to facilitate  $\text{Li}^+$  transport among active material particles. The interconnected  $\text{Li}^+$  transport pathways from the bottom of the electrode to the surface leads to a significant reduction in the electrolyte/electrode impedance.<sup>36,72</sup> Hence, improved electrochemical performance can be expected. For instance, Duan *et al.* polymerized poly(ethylene glycol) methyl ether acrylate *in situ* on the interface of a LLZO/LFP cathode, forming a  $5.7 \text{ }\mu\text{m}$  SPE on the surface (Fig. 4G).<sup>72</sup> With the introduction of the SPE layer, both the bulk resistance and charge-transfer resistance were reduced, enabling the assembled Li-LFP SSLB to stably cycle for 120 cycles with a high capacity retention of 94.5%. In another case, Wang's group developed a two-step slurry coating method and coated SPE solution on a LFP cathode (labeled cathode-supported SPE).<sup>36</sup> The results showed that the SPE can wet both the surface and internal particles of the LFP cathode, thus significantly reducing the interfacial resistance. Moreover, by avoiding delamination of SPE from the substrate, the SPE thickness can be reduced to  $9.5 \text{ }\mu\text{m}$ . The Li-LFP SSLB assembled with cathode supported SPE demonstrated improved rate-performance compared with conventional electrodes due to the reduced interfacial resistance and thin SSE (Fig. 4H). Additionally, a battery pack made of 3 SSLB units was assembled and integrated in a coin cell format, which delivered an open circuit voltage of 9.12 V, demonstrating its potential for practical application.

Besides the aforementioned SPEs, some thin ceramic SSEs have also been reported in Li-LFP SSLBs. Wang and co-workers demonstrated that an ultrathin LLTO SSE can be realized by a tape casting technique (Fig. 4I). According to their simulations, such a thin LLTO SSE ( $25 \text{ }\mu\text{m}$ ) applied in Li-LFP SSLBs has the potential to deliver a high energy density of over  $300 \text{ W h kg}^{-1}$ . In practical application, due to the relatively low ionic conductivity of  $2.0 \times 10^{-5} \text{ S cm}^{-1}$ , the assembled cells should be operated at a high temperature of  $65 \text{ }^\circ\text{C}$ . As shown in Fig. 4J, the Li-LFP cell delivers capacities of over  $150 \text{ mA h g}^{-1}$  and  $55 \text{ mA h g}^{-1}$  at 0.1C and 0.5C, respectively.<sup>41</sup> This work

demonstrated that thin oxide SSE-based SSLBs are possible. Of course, further improving the electrochemical performance is needed by enhancing the ionic conductivity and building better interfaces.

**2.3.2 Solid-state Li-LCO and Li-NMC batteries.** One of the main goals for SSLBs is to increase the potential energy density of the battery system. Compared with the Li-LFP system, SSLBs coupled with high-voltage cathodes such as LCO and NMC are more beneficial towards achieving higher energy densities. Nevertheless, these cathodes introduce new challenges, especially with respect to the ESWs of the SSEs. Generally speaking, a relatively high oxidation stability of over 4.2 V is required for compatibility with these cathodes. Most oxide- and halide-based SSEs show good stability towards high voltages and can be directly used as the SSEs in conjunction with high-voltage cathode materials.<sup>8,15</sup> With this in mind, the primary issues of oxide/halide type SSEs are associated with the interface and anode stability. However, PEO-based SPEs and sulfide SSEs still can't tolerate a voltage of over 4 V, which hinders their compatibility with LCO and NMC cathode materials.<sup>88,89</sup> Until now, the application of ultrathin SSEs in high-voltage SSLBs has remained challenging. For SPEs, one of the most widely adopted strategies to enable PEO-based SPEs in high voltage SSLBs is through the introduction of another high-voltage compatible SPE towards the cathode. For instance, Guo's group proposed a heterogeneous multilayered solid electrolyte (HMSE) with oxidation-resistant poly(acrylonitrile) (PAN)/reduction-resistant polyethylene glycol diacrylate (PEGDA) for the cathode and anode, respectively, with a  $\text{PAN@Li}_{1.4}\text{Al}_{0.4}\text{Ge}_{1.6}(\text{PO}_4)_3$  (LAGP, 80 wt%) intermediate layer to inhibit Li dendrite penetration (Fig. 5A). Benefitting from the combined functionality of each SPE layer, the HMSE with a thickness of  $25 \text{ }\mu\text{m}$  presented excellent high-voltage performance in Li-NMC cells (operating voltage window: 2.8–4.3 V). At a C-rate of 0.2C, the assembled Li-NMC-811 cell exhibited a high initial capacity of  $184 \text{ mA h g}^{-1}$  and a capacity retention of 94.4% after 175 cycles.<sup>90</sup> In another study, Cui's group extended the electrochemical window of PEO SPE *via* modification of the Li salt composition. They found that  $\text{Li}[(\text{CF}_3)_3\text{COBF}_3]$  (LITFPFB) salt is beneficial for building a solid-electrolyte interlayer (SEI) on the anode surface and another cathode-electrolyte interface (CEI) on the cathode surface (Fig. 5B), thus realizing the stable use of PEO ( $40 \text{ }\mu\text{m}$ ) in a Li-LCO SSLB at 4.3 V.<sup>91</sup>

Despite its positive effect in enhancing the electrochemical performance of high-voltage SSLBs, the multi-layered structure will no doubt increase the difficulty and cost of manufacturing thin SPEs. Moreover, the multi-layered structure will increase the thickness of SPEs and have negative effects on energy density. With this in mind, our group found that the terminal -OH group in PEO-based SPEs is the limiting factor of the ESW. Replacing the terminal -OH groups with more stable functional groups can further extend the ESW, enabling the application of PEO-based SPEs in high-voltage SSLBs. For instance, we found that replacing the -OH groups in polyethylene glycol (PEG) SPE with -OCH<sub>3</sub> groups (the polymer is labeled PEGDME) can extend the oxidation stability voltage from 4.05 V to 4.3 V (Fig. 5C).

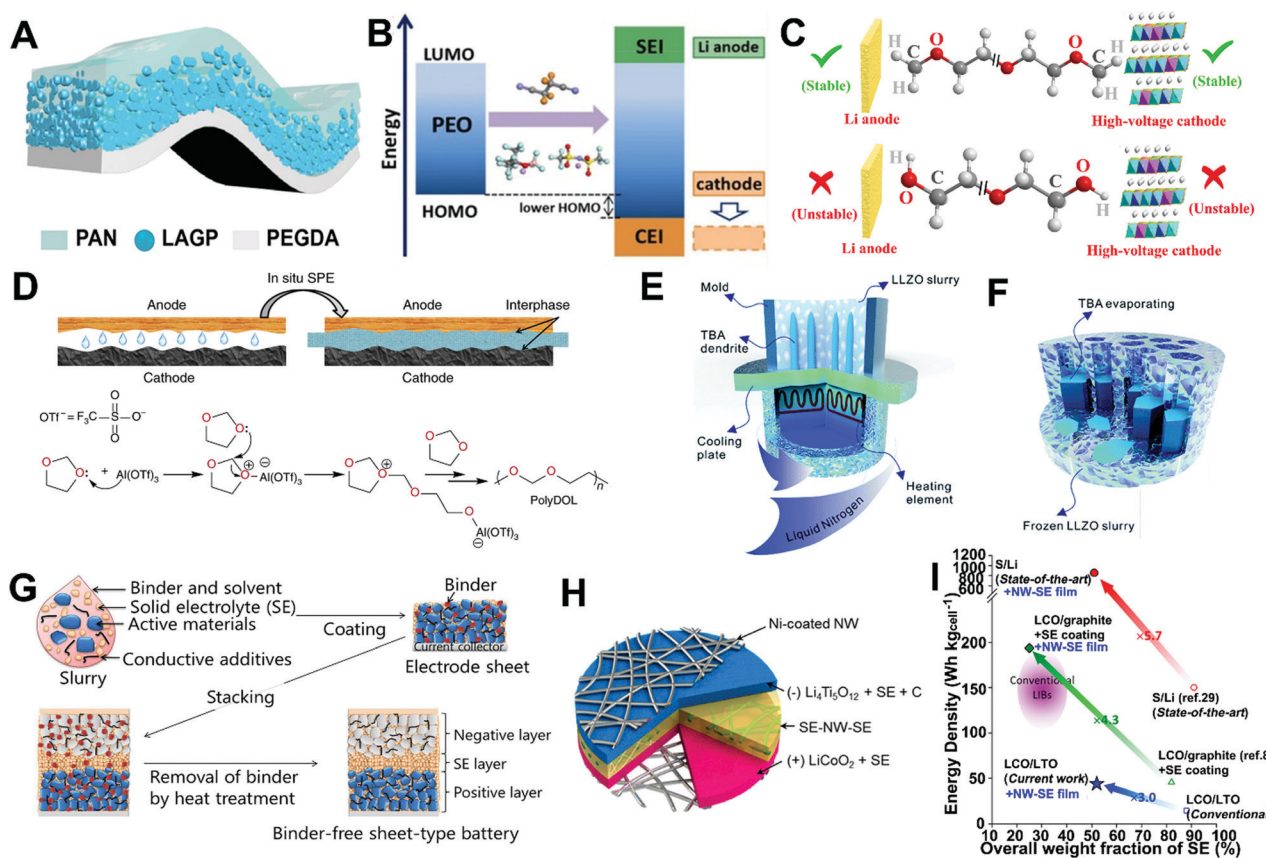


Fig. 5 (A) Schematic diagram of the HMSE. Reproduced with permission from ref. 90. Copyright (2019) Wiley-VCH. (B) Schematic illustration of the role of LITFPFB in extending the ESW via the formation of a SEI and a CEI. Reproduced with permission from ref. 91. Copyright (2019) Wiley-VCH. (C) Schematic illustration of PEGDME and PEG response to the Li anode and high voltage. Reproduced with permission from ref. 88. Copyright (2020) Royal Society of Chemistry. (D) Schematic of *in situ* polymerizing polyDOL and the relevant polymerization mechanism. Reproduced with permission from ref. 73. Copyright (2019) Nature Publishing Group. Schematics of the (E) freeze casting apparatus and (F) formation of the porous LLZO by freeze drying. Reproduced with permission from ref. 92. Copyright (2019) Royal Society of Chemistry. (G) Schematic diagram showing the fabrication process for binder-free sheet-type SSLBs. Reproduced with permission from ref. 93. Copyright (2018) Nature Publishing Group. (H) Schematic diagram of a free-standing LCO-LTO SSLB. (I) The energy density of the SSLB as a function of the overall weight fraction of SE varied by electrode chemistry, the presence of SE coating, and a NW-SE film. Reproduced with permission from ref. 53. Copyright (2015) American Chemical Society.

The high oxidation stability is suitable for realizing the combination of PEGDME SPE with high voltage cathodes. The Li-NMC532 cell assembled with PEGDME SPE (thickness: 50  $\mu\text{m}$ ) delivered a high capacity of over 120  $\text{mA h g}^{-1}$  and a high capacity retention of 80 wt% after 100 cycles at 0.2C (operating voltage window: 2.5–4.3 V). In contrast, only a capacity of 19  $\text{mA h g}^{-1}$  was retained after 100 cycles and a serious increase in overpotential can be observed during cycling for its counterpart (PEG SPE).<sup>88</sup> In addition, some new SPEs with higher ESWs have been developed to improve compatibility with high-voltage cathodes. For instance, Archer's group developed poly(1,3-dioxolane), labeled polyDOL, via *in situ* ring-opening polymerization of DOL with the assistance of  $\text{Al}(\text{OTf})_3$  initiator (Fig. 5D). The results showed that the polyDOL SPE exhibited a high oxidation stability of greater than 5 V, enabling the assembled Li-NMC622 cell to stably cycle for over 700 cycles at 1C.<sup>73</sup>

Recently, some thin ceramic SSE-based high-voltage SSLBs have also been reported by coupling thin SSE preparation

technology innovation and functional/structural innovation with SSEs/cathode materials. Compared with SPEs, oxide SSEs have higher oxidation stability windows, which enables their compatibility with high-voltage cathodes. As mentioned in Section 2.1.2, tape casting is a good method to achieve thin oxide SSEs with thicknesses less than 100  $\mu\text{m}$ . However, the fabrication of a thin SSE through this method is not enough on its own to drive good electrochemical performance. It is necessary to construct interconnected  $\text{Li}^+$  transport channels in the cathode to facilitate  $\text{Li}^+$  transport and ensure high capacity output, especially for electrodes with high active material loadings. With this in mind, Shen *et al.* developed a freeze casting technique to obtain a porous LLZO pellet with vertically-aligned channels, which acted as an interconnected  $\text{Li}^+$  conductive host for the infusion of active materials. During the synthesis process, *tert*-butyl alcohol (TBA) was chosen as the solvent, which could be frozen in place and functioned as the *in situ* template (Fig. 5E). After evaporating the TBA solvent, a porous LLZO pellet with vertically-aligned channels was

obtained (Fig. 5F). Coupling the porous LLZO host with a NMC622 cathode and a dense LLZO film (20  $\mu\text{m}$ ) obtained by tape casting, oxide SSE-based Li-NMC622 cells demonstrated good electrochemical performance. With an ultrahigh NMC622 loading of 15.7  $\text{mg cm}^{-2}$ , the cells delivered an initial capacity of 175  $\text{mA h g}^{-1}$  and a high capacity retention of 72% after 90 cycles, even with a high cutoff voltage of 4.7 V.<sup>92</sup> Among the various types of SSEs, sulfide-based SSEs possess the highest ionic conductivities and are regarded as one of the most promising candidates for the realization of SSLBs operating at low temperatures. However, their narrow ESWs significantly hinder their practical applications. Prevention of direct contact between SSEs and high-voltage cathode materials with protective coating layers on cathode materials is currently the most popular and effective strategy to stabilize sulfide-based SSEs.<sup>27,94</sup> For instance, as shown in Fig. 5G, Yamamoto *et al.* developed a binder-free sheet-type SSLB with a multi-step slurry coating process followed by removal of the binder with a heat treatment. On the cathode side, the NMC111 cathode materials are protected with a  $\text{LiNbO}_3$  coating to prevent the side reactions between sulfide SSE and NMC111. Benefitting from the reduced interfacial resistance with the continuous casting process and suppressed side reactions, the assembled NMC111/ $\text{Li}_3\text{PS}_4$ /Li-In cell delivered a high initial capacity of 149  $\text{mA h g}^{-1}$  and a high capacity retention of 84% after 175 cycles. The operating voltage window is 2.0–3.7 V, corresponding to a voltage window of 2.6–4.3 V vs.  $\text{Li}^+/\text{Li}$ .<sup>93</sup> Moreover, the binder-free SSE structure showed advantages in  $\text{Li}^+$  transport and enhanced the rate performance of SSLBs. The SSLBs using binder-free SSE delivered a high capacity of roughly 100  $\text{mA h g}^{-1}$  at 1.5  $\text{mA cm}^{-2}$ , which is double that of the binder-containing SSE, and are expected to achieve higher power density for practical application. Despite the achievements using thin SSE in high-voltage SSLBs, few examples of successful integration of Li metal anodes exist. Using alternative Li alloys or other anode materials will no doubt reduce the energy density. For instance, Jung's group developed a nonwoven (NW) scaffold-reinforced  $\text{Li}_3\text{PS}_4$  film (labeled NW-SE) with a thickness of 70  $\mu\text{m}$  and applied it as the electrolyte in a  $\text{Li}_4\text{Ti}_5\text{O}_{12}$  (LTO)–LCO system (Fig. 5H). Despite the relatively high LCO and LTO loadings of 10.5  $\text{mg cm}^{-2}$  and 12  $\text{mg cm}^{-2}$  used in this system, only a low energy density of less than 50  $\text{W h kg}^{-1}$  can be realized (Fig. 5I). If the LCO cathode is combined with a graphite anode, the energy density can be further increased to around 200  $\text{W h kg}^{-1}$ . Alternatively, replacing the cathode and anode materials with sulfur and Li metal, respectively, can lead to ultrahigh energy densities greater than 900  $\text{W h kg}^{-1}$ .<sup>53</sup> In this regard, the use of a thin SSE is still not enough to achieve high energy density. Thus, the combination of thin SSEs with a Li metal anode and a rationally designed SSLB structure is required to ensure high electrochemical performance output.

**2.3.3 Solid-state Li–S batteries.** The SSLSB is another high-energy-density system (theoretical energy density: 2600  $\text{W h kg}^{-1}$ ) based on the multi-electron reaction of active sulfur. According to their different reaction mechanisms, SSLSBs can be categorized into two systems: solid–liquid dual-phase reaction systems and

solid-phase reaction systems.<sup>4</sup> Generally, in SSLSBs, solid–liquid dual-phase reactions can only occur in SPE and SPE-based hybrid systems, while a polysulfide-free solid-phase reaction occurs in ceramic SSE systems. However, due to their rigidity, most oxide SSEs can't be used as single components in SSLSBs, and a small amount of liquid electrolyte or SPE is required to modify the interface, and thus induce the transfer from a solid-phase reaction into a solid–liquid dual-phase reaction. In SSLSBs, the issues of polysulfide shuttling and mismatched interfaces are of significance. Many strategies have been developed to solve the aforementioned issues, which has been summarized well in previous reviews.<sup>4,95</sup> Herein, we only briefly introduce some solutions that have been used in conjunction with thin SSE-based SSLSBs (typically SSE < 100  $\mu\text{m}$ ).

In SPE-based SSLSBs, the issues associated with interfacial contact are not as problematic as those observed in ceramic systems. Rather, the critical issue is the polysulfide shuttling due to the high solubility of polysulfides in the polymer matrix. To solve this issue, the introduction of polar functional groups has been widely adopted, where the polar function groups are capable of adsorbing polysulfide species and preventing their shuttling. Moreover, various polar functional group-containing ceramic fillers/additives have proven to be effective in SPE systems and serve multiple functionalities. Firstly, the introduction of ceramic SSEs can enhance the mechanical strength, which helps suppress Li dendrite formation. Secondly, ceramic SSE fillers induce higher ionic conductivities. Lastly, similar to other additives/fillers, the polar functional groups on their surfaces promote polysulfide shuttling suppression. For instance, as shown in Fig. 6A, Tao *et al.* reported the incorporation of LLZO as a filler into a PEO SPE and realized high-performance SSLSBs operating at 37  $^\circ\text{C}$ . By optimizing the filler content in the SPE, they found that the PEO electrolyte with 15 wt% LLZO filler achieved the highest ionic conductivities, which are  $1.1 \times 10^{-4} \text{ S cm}^{-1}$  at 40  $^\circ\text{C}$  and  $1.9 \times 10^{-3} \text{ S cm}^{-1}$  at 70  $^\circ\text{C}$ . Benefitting from the improved ionic conductivity and polysulfide shuttling suppression, the assembled SSLSBs with a S@LLZO@C cathode delivered a reversible capacity of around 900  $\text{mA h g}^{-1}$  and a high coulombic efficiency (CE) of 100% within 200 cycles at 0.05C.<sup>96</sup> Another method of suppressing polysulfide shuttling is through the addition of electrolyte additives into SPEs which can modify the SEI. As shown in Fig. 6B, lithium bis(fluorosulfonyl)imide (LiFSI) instead of the widely used bis(trifluoromethanesulfonyl)imide (LiTFSI) was chosen as the Li salt for SPE preparation. The results showed that LiFSI is capable of forming a more stable SEI on the anode surface, thus alleviating polysulfide shuttle and achieving high CEs during cycling. In contrast, overcharging was observed for SSLSBs assembled with LiTFSI salt.<sup>97</sup> In another study,  $\text{LiN}_3$  was proposed as an electrolyte additive by Armand's group. According to their concept,  $\text{LiN}_3$  can be oxidized into  $\text{N}_2$  on the cathode, which can then shuttle across the electrolyte to form an ionically conductive layer ( $\text{Li}_3\text{N}$ ) on the Li anode surface (Fig. 6C). Even though LiTFSI was used as the Li salt, the assembled SSLSBs still delivered high CEs and a reversible discharge capacity of approximately 800  $\text{mA h g}^{-1}$  after 30 cycles.<sup>98</sup>

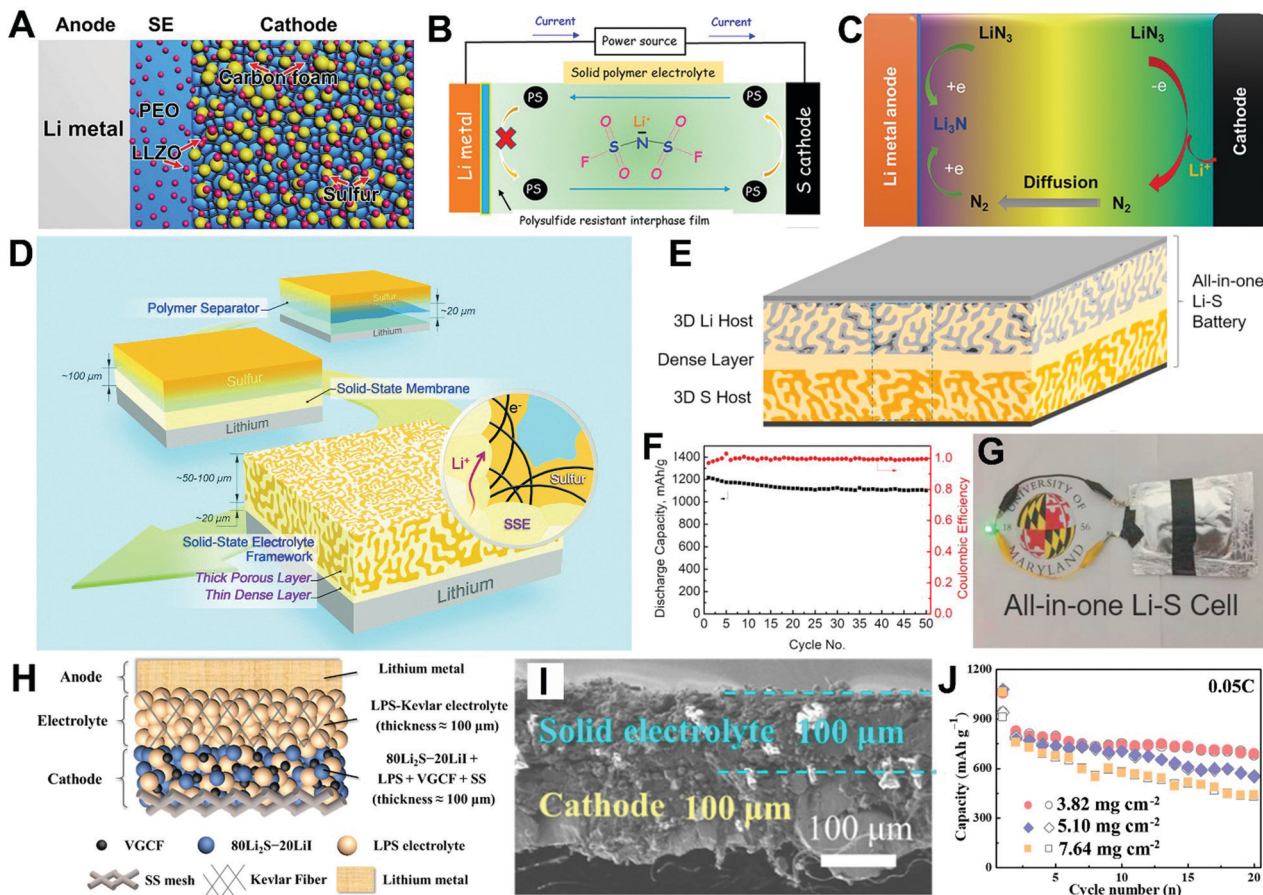


**Fig. 6** (A) Schematic illustration of a SSLSB based on PEO–LLZO hybrid electrolyte. Reproduced with permission from ref. 96. Copyright (2017) American Chemical Society. (B) Schematic illustration of SSLSBs with LIFSI as Li salt. Reproduced with permission from ref. 97. Copyright (2017) American Chemical Society. (C) Schematic illustration of electrochemical reactions in SSLSBs with  $\text{LiN}_3$  additive. Reproduced with permission from ref. 98. Copyright (2017) Wiley-VCH. (D) Schematic of the novel bilayer solid-state electrolyte framework in comparison with traditional soft polymer separators ( $\sim 20 \mu\text{m}$ ) and rigid solid-state membrane architectures ( $\sim 100 \mu\text{m}$ ). Reproduced with permission from ref. 44. Copyright (2017) Royal Society of Chemistry. (E) Schematic illustration and (F) cycling performance of all-in-one SSLSBs. (G) Optical photograph of an all-in-one SSLSB soft package. Reproduced with permission from ref. 45. Copyright (2018) Elsevier. (H) Schematic of a cathode-supported SSLSB. (I) SEM image of the cathode-supported SSLSBs with various  $\text{Li}_2\text{S}$  loadings. Reproduced with permission from ref. 54. Copyright (2019) American Chemical Society. (J) Electrochemical performance of cathode-supported SSLSBs with various  $\text{Li}_2\text{S}$  loadings. Reproduced with permission from ref. 54. Copyright (2019) American Chemical Society.

Limiting the polysulfide shuttling effect *via* the addition of inorganic fillers and electrolyte additives has proven to be effective in improving the cycling stability of SPE-based SSLSBs. However, due to the slow diffusion rate of polysulfides in SPEs and the electronically insulating nature of SPEs, polysulfides anchored in the polymer matrix can't participate in electrochemical reactions and lead to active material loss and capacity decay. With this in mind, oxide SSEs have been proposed as physical barriers to inhibit polysulfide diffusion. Of the various oxide SSEs, garnet-type SSEs typically show higher stability than NaICON-type (LATP, LAGP) and perovskite-type (*e.g.* LLTO) SSEs. Hence, many researchers have focused on the application of garnet SSEs in SSLSBs. For instance, Hu's group proposed a bi-layered LLCZNO SSE with a porous layer sintered on a dense supporting electrolyte (Fig. 6D). The bi-layered structure was fabricated by tape-casting. The thicknesses of the porous layer and dense layer were controlled to be  $35 \mu\text{m}$  and  $70 \mu\text{m}$ , respectively. The dense electrolyte layer functioned as a physical

barrier to suppress polysulfide shuttling, while the porous structure was applied as a host for sulfur accommodation and liquid electrolyte infusion. As a result, with a high sulfur loading of  $7.5 \text{ mg cm}^{-2}$ , the assembled SSLSB delivered a capacity of around  $600 \text{ mA h g}^{-1}$  as well as a high average CE of 99% at  $0.2 \text{ mA cm}^{-2}$ .<sup>44</sup> In another case, a similar bi-layered LLZO structure was reported by Wachsmann's group, where a porous LLZO textile was fabricated by a templating method. Due to the interconnected  $\text{Li}^+$  conductive network built with the LLZO fibers, the assembled SSLSB exhibited improved electrochemical performance. The assembled SSLSB delivered a reversible capacity of over  $1000 \text{ mA h g}^{-1}$  after 40 cycles at 0.1C, when the sulfur loading was  $10.8 \text{ mg cm}^{-2}$ . Upon further increasing the sulfur loading to  $18.6 \text{ mg cm}^{-2}$ , a high capacity of over  $800 \text{ mA h g}^{-1}$  was maintained. The high performance obtained with a thin SSE ( $20 \mu\text{m}$ ) makes it possible to achieve a high energy density of  $352 \text{ W h kg}^{-1}$ .<sup>99</sup>

To further decrease the interfacial resistance, an all-in-one SSLSB was reported with a porous–dense–porous layered

structure for Li melting and sulfur infusion (Fig. 6E).<sup>45,46</sup> Interestingly, the results showed that the thickness of the dense/porous structure can be controlled within the range of  $\sim 15/50\text{--}70\ \mu\text{m}$ , respectively. The all-in-one structure showed several advantages in terms of  $\text{Li}^+/\text{e}^-$  transport, low localized current densities, volume change confinement and cell manufacturing. As a proof of concept, a high discharge capacity of  $1200\ \text{mA h g}^{-1}$  was realized by  $5.4\ \text{mg cm}^{-2}$  sulfur loaded SSLSBs with less than  $1\ \mu\text{L mg}^{-1}\ \text{S}$  within 50 cycles (Fig. 6F). Moreover, the potential of an all-in-one structure for practical application was also proven through pouch cell manufacturing (Fig. 6G).<sup>45</sup>

Compared with the aforementioned SSLSB systems, the sulfide SSE-based SSLSB is a polysulfide-free system, where the sulfur is directly reduced to  $\text{Li}_2\text{S}$  during discharge. The biggest challenge that hinders its application is its large interfacial resistance. To solve this problem, Wang and coworkers developed a cathode-supported SSLSB (Fig. 6H) with a thin  $\text{Li}_3\text{PS}_4$  SSE ( $100\ \mu\text{m}$ , Fig. 6I). As mentioned in Section 2.3.1, a cathode-supported structure can significantly reduce the resistance of the electrolyte/electrode interface, thus enhancing electrochemical performance. As shown in Fig. 6J, the  $3.82$ ,  $5.10$ , and  $7.64\ \text{mg cm}^{-2}$   $\text{Li}_2\text{S}$ -loaded SSLSBs delivered a high initial capacity of around  $900\ \text{mA h g}^{-1}$  at  $0.05\text{C}$ , corresponding to high areal capacities of  $3.59$ ,  $4.80$  and  $6.97\ \text{mA h cm}^{-2}$ . According to their simulations, the SSLSB assembled with a  $7.64\ \text{mg cm}^{-2}$   $\text{Li}_2\text{S}$  cathode has the potential to deliver a high energy density of  $370.6\ \text{W h kg}^{-1}$ .<sup>54</sup> However, it should be noted that the cycling performance is still insufficient. More effort should be focused on addressing the cycling stability, understanding the structure/interface change and structure–performance relationships.

**2.3.4 Solid-state Li–O<sub>2</sub> batteries.** Solid-state Li–O<sub>2</sub> batteries (SSLOBs) are different from the previously discussed SSLB systems and have open cell configurations to allow external O<sub>2</sub> to penetrate the cathode side and act as an active material source. Due to their different reaction mechanisms, the structural design of SSLOBs shows several new features. (1) A porous electrode. Unlike other SSLBs, where the active materials are directly added into the slurry during electrode preparation, the discharge product ( $\text{Li}_2\text{O}_2$ ) is formed *in situ* during electrochemical cycling. With this in mind, a porous electrode is essential to accommodate the discharge product. (2) Construction of dual  $\text{Li}^+$  and electron conductors. In general, the electrochemical reactions can only occur at the tri-phase interface of the active material,  $\text{Li}^+$  conductor and electronic conductor. Hence, building an effective tri-phase interface is required for promoting the electrochemical reactions. In the SSLOB system, active O<sub>2</sub> is provided through an external environment, which can react with  $\text{Li}^+$  at the phase boundary of the  $\text{Li}^+$  conductor and electronic conductor. (3) High-oxidation-resistance SSE. The discharge plateau of SSLOBs is around  $4.2\text{--}4.3\ \text{V}$ . In order to achieve high cycling stability, the SSE should tolerate a high voltage of at least  $4.3\ \text{V}$ . Moreover, it should be chemically inert to O<sub>2</sub>, which is another issue that needs to be overcome for some electrolyte systems. Due to the aforementioned issues, the development of SSLOBs has been much slower than the other systems and is still in an early exploration stage.

Among the various SSEs, oxide SSEs with wide ESWs and air stability show promising application in SSLOBs.<sup>100–102</sup> The configuration of SSLOBs is similar to that of oxide SSE-based SSLSBs in Section 2.3.3. As shown in Fig. 7A, a dense oxide SSE (LAGP) is used to transport  $\text{Li}^+$  and separate the anode from the

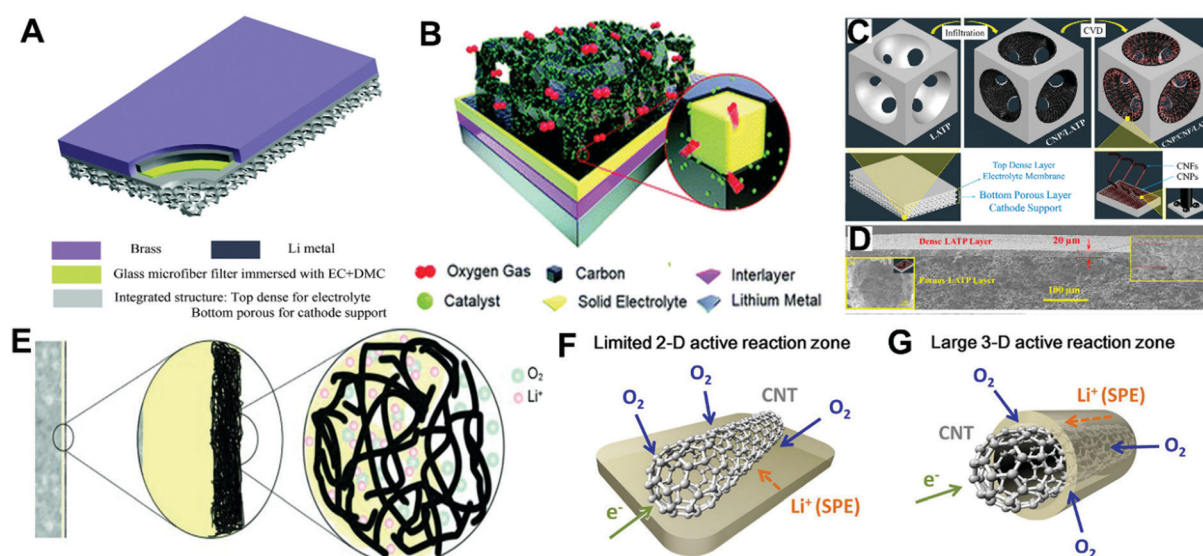


**Fig. 7** (A) Schematic illustration of a SSLOB with a LATP SSE. Reproduced with permission from ref. 102. Copyright (2015), Royal Society of Chemistry. (B) Schematic illustration of a SSLOB with CoO catalyst. Reproduced with permission from ref. 100. Copyright (2019) Royal Society of Chemistry. (C) Schematic illustration of *in situ* growing CNTs in the porous LATP. (D) SEM images of a bi-layer LATP structure. Reproduced with permission from ref. 101. Copyright (2016) Elsevier. (E) Schematic illustration of a liquid-free SPE-based SSLOB. Reproduced with permission from ref. 103. Copyright (2015) Wiley-VCH. Comparison of (F) a limited 2D active reaction zone in a conventional CNT and SPE sandwiched structure with (G) an enlarged 3-D active reaction zone in a 3-D CNT/SPE architecture. Reproduced with permission from ref. 104. Copyright (2014) Nature Publishing Group.

cathode while suppressing O<sub>2</sub> diffusion. A porous oxide SSE layer with a thin carbon coating is applied as the cathode, which supplies space for electrochemical reactions and discharge product accommodation. Based on the high ionic conductivity of LAGP SSE (36 μm) and dual-phase interface construction, a SSLOB delivered a high discharge capacity of 14 200 mA h g<sup>-1</sup> carbon at 0.15 mA cm<sup>-2</sup>, and could sustain 100 cycles at a fixed capacity of 1000 mA h g<sup>-1</sup> carbon.<sup>102</sup> To further improve the electrochemical kinetics, Park's group developed a CoO catalyst. SSLOBs with a thin LLTO SSE (thickness: 19.8 μm, Fig. 7B) showed good cycling stability for 132 cycles at a current density of 500 mA h g<sub>C+CoO</sub><sup>-1</sup>.<sup>100</sup> To avoid detachment of the electronic conductor SSE that would limit the cycling life of SSLOBs, Zhao's group developed a chemical vapor deposition (CVD) method to grow CNTs *in situ* on the surface of porous LATP (Fig. 7C). The stable dual-phase interface enabled Li<sup>+</sup>/e<sup>-</sup> with fast transport pathways. As a result, SSLOBs with a 20 μm LATP SSE (Fig. 7D) delivered excellent cycling stability for 1174 cycles (150 days) in O<sub>2</sub> and 450 cycles (75 days) with degradation of <3% in ambient air (with RuO<sub>2</sub> and NiO as the catalysts). Moreover, the charge/discharge rate reached as high as 15 mA cm<sup>-2</sup>, which is 2–4 orders of magnitude higher than that of conventional SSLOBs.<sup>101</sup>

Besides oxide SSE-based SSLOBs, a few reports have focused on SPE-based SSLOBs. As an example, Balaish *et al.* developed a PEO SPE-based SSLOB (Fig. 7E). At 80 °C, where PEO SPE (thickness: 150 μm) has an acceptable ionic conductivity, the SSLOB displayed a higher cell discharge voltage of ~80 mV compared to liquid electrolyte (1 M lithium triflate/triethylene glycol dimethyl ether)-based SSLOBs.<sup>103</sup> The above successes provide key evidence that SPE-based SSLOBs deserve to be considered as promising battery systems for EVs due to their high energy density and safety.

As previously mentioned, in SSLOBs, the construction of a porous cathode with a dual-phase interface is of significance to enhance the discharge capacity and cycling life. With this in mind, Byon's group developed a SSLOB based on a 3D structured CNT/SPE (Fig. 7G), where the void spaces in the porous CNT/SPE film afford an enlarged interfacial reaction zone for Li<sup>+</sup>, O<sub>2</sub> gas and electrons. Thus, a larger discharge capacity is obtained for the 3D structured CNT/SPE cell than the conventional CNT and SPE sandwiched structure which had a limited 2D active reaction zone (Fig. 7F).<sup>104</sup> Additionally, SPEs with high ionic conductivity are critical to achieving high capacity output. A plasticized PEO-based SPE (named PPE) with increased ionic conductivity was proposed to improve the electrochemical performance of SSLOBs. Accordingly, the as-prepared PPE displayed an almost linear trend and conductivity values ranging from 3 × 10<sup>-4</sup> S cm<sup>-1</sup> to around 10<sup>-3</sup> S cm<sup>-1</sup> in the temperature window of 25 °C to 95 °C. As a result, a SSLOB delivered a good cycling stability of over 20 cycles at 100 mA g<sup>-1</sup> with a limited capacity of 500 mA h g<sup>-1</sup>. Moreover, practical energy densities greater than 300 W h kg<sup>-1</sup> could be achieved through battery optimization.<sup>105</sup> Despite these great achievements, decomposition of SPEs under high voltages due to their narrow ESWs should be taken into consideration. Moreover, their

semi-molten state, especially at high operating temperatures, will block the porous channels.

**2.3.5 Solid-state lithium pouch cells.** As promising energy storage systems, SSLBs are aimed to supply energy to portable electronic devices and EVs. Therefore, it is of great significance to find suitable processing techniques for mass production. Compared with coin cells and model cells, pouch cells are more suitable for the evaluation of fabrication techniques' potential in industry application. Recently, some thin SSE-based pouch cells have been reported and have demonstrated excellent electrochemical performance. For instance, as shown in Fig. 8A, the researchers from the Institut de Recherche Hydro-Québec reported a 3.8 cm<sup>2</sup> Li-LFP SSLB pouch cell, where a 29 μm polyether-LiTFSI SPE worked as the SSE and a 46 μm Li foil functioned as the anode. The small pouch cell demonstrated 80% capacity retention with over 1400 cycles at C/3.<sup>106</sup> In another study, Sakuda *et al.* reported a 22 × 22 mm<sup>-2</sup> graphite-NMC111 pouch cell with an ~50 μm Li<sub>3</sub>PS<sub>4</sub> SSE based on a conventional slurry coating method. With a high capacity of over 1.5 mA h cm<sup>-2</sup>, the graphite-NMC111 pouch cell delivered an energy density of 155 W h kg<sup>-1</sup>, where the weight of the current collectors and the exterior package was excluded from the weight for calculation.<sup>40</sup> The slurry coating method was further adopted by Jung's group for the fabrication of graphite-NMC622 pouch cells. With a thinner Li<sub>6</sub>PS<sub>5</sub>Cl SSE, an 80 × 60 mm<sup>2</sup> SSLB pouch cell delivered a gravimetric energy density of 184 W h kg<sup>-1</sup> and a volumetric energy density of 432 W h L<sup>-1</sup>.<sup>107</sup> To further enhance the energy density and realize the combination of a Li anode with high voltage cathodes, our group developed a PEGDME SPE with an improved oxidation resistance and combined it with a NMC532 cathode. As shown in Fig. 8B, the assembled Li-NMC532 pouch cell demonstrated a high capacity retention of 90% after 110 cycles with a negligible overpotential increase at 0.2C (Fig. 8C). In another study, Guo's group applied the HMSE discussed in Section 2.3.2 as the SSE and assembled a Li-NMC-811 SSLB pouch cell. Benefitting from the extended ESW, the Li-NMC-811 SSLB pouch cell showed a highly reversible capacity of 191 mA h g<sup>-1</sup> within 10 cycles at 0.1C.<sup>90</sup> To avoid using Li alloy or graphite that would reduce the energy density of the cells, researchers from Samsung Electronics Co., Ltd, developed an anode-free SSLB pouch cell. In their case, a Ag-C composite layer on the anode side was used to regulate Li deposition. Accordingly, a dense Li layer could be repeatedly formed and dissolved between the Ag-C composite and anode current collector. Moreover, Ag nanoparticles were alloyed with Li in the early stage of the charging process, but a significant fraction of Ag was found to migrate towards the current collector and assist the uniform and dendrite-free plating of Li metal. As a result, a 0.6 A h Li-NMC9.5.5 (active area: 6.7 × 11.2 cm<sup>2</sup>, Fig. 8D) SSLB pouch cell assembled with a 30 μm Li<sub>6</sub>PS<sub>5</sub>Cl SSE exhibited a high energy density (>900 W h L<sup>-1</sup>), stable CE (over 99.8%) and long cycling life (1000 cycles, Fig. 8E).<sup>23</sup>

Compared with Li-ion SSLBs, SSLSBs have the potential to deliver higher energy density due to the high theoretical capacity of sulfur. Recently, some SSLSB pouch cells using thin

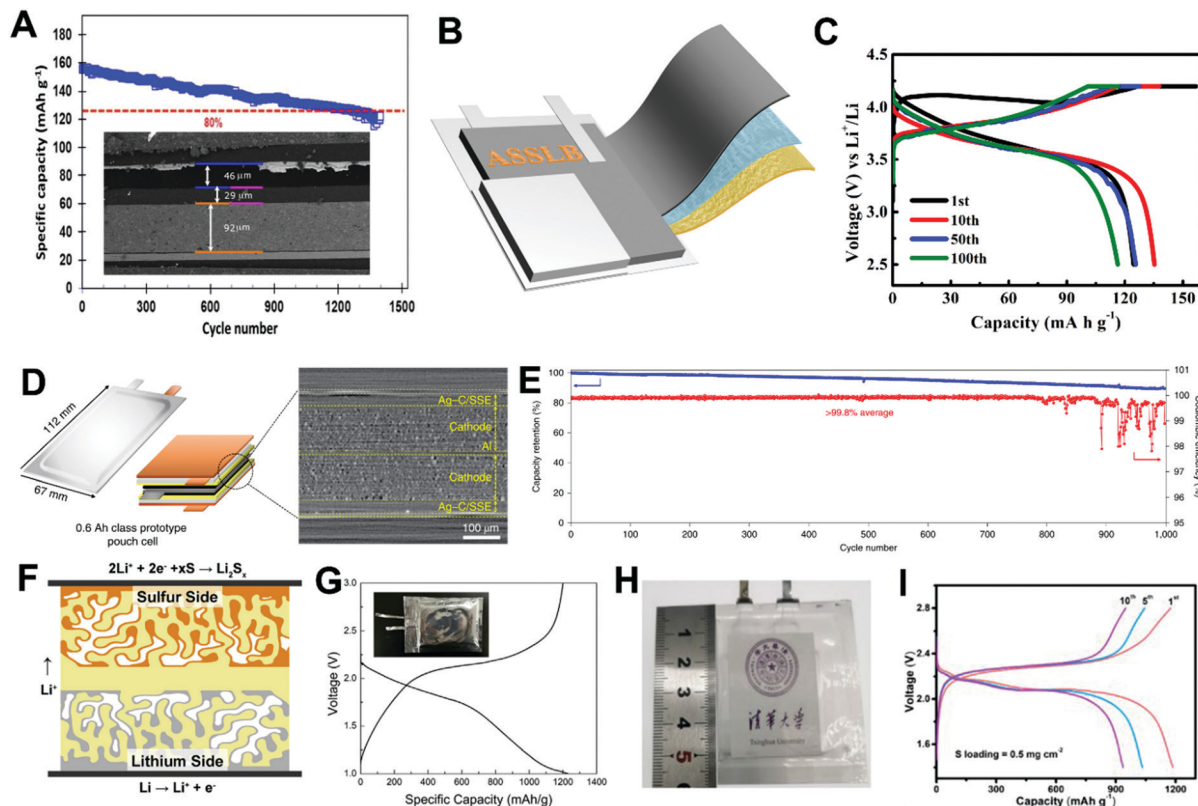


**Fig. 8** (A) Cycling stability of a Li–LFP SSLB pouch cell at C/3; the inset shows a cross-sectional SEM image of the cell. Reproduced with permission from ref. 106. Copyright (2015) American Chemical Society. (B) Schematic illustration and (C) charging–discharging profiles of a Li–NMC532 SSLB pouch cell assembled with a PEGDME SPE. Reproduced with permission from ref. 88. Copyright (2020) Royal Society of Chemistry. (D) Schematic illustration and X-ray computed tomography and (E) cycling stability of a 0.6 Ah Li–LiNi<sub>0.90</sub>Mn<sub>0.05</sub>Co<sub>0.05</sub>O<sub>2</sub> SSLB pouch cell. Reproduced with permission from ref. 23. Copyright 2020, Nature Publishing Group. (F) Schematic illustration of a Li–S trilayer cell. (G) Charging–discharging profile of a Li–S trilayer pouch cell. Reproduced with permission from ref. 46. Copyright (2019) Elsevier. (H) Optical image and (I) charging–discharging profiles of a SSSLB pouch cell based on a slurry coating method. Reproduced with permission from ref. 37. Copyright (2020) Elsevier.

oxide- and sulfide-SSEs have already been reported. For instance, Wachsman's group developed a tri-layered garnet-based SSE with a dense layer sandwiched between two porous layers. As shown in Fig. 8F, the dense middle layer (20  $\mu\text{m}$ ) acted as the SSE, while the porous layers (50  $\mu\text{m}$ ) functioned as the hosts for Li and sulfur accommodation. Benefitting from the "all-in-one" feature, the pouch cell could be easily sealed in a pouch cell. The SSLB pouch cell demonstrated a high reversible capacity of over 1200  $\text{mA h g}^{-1}$  within 8 cycles at 0.1C (Fig. 8G).<sup>46</sup> In another study, Zhang and his coworkers developed a  $33 \times 33 \text{ mm}^2$  sulfide-SSE-based Li–S SSLB pouch cell *via* a slurry coating method. With a  $\text{Li}_6\text{PS}_5\text{Cl}$  SSE thickness of 380  $\mu\text{m}$ , the assembled Li–S SSLB pouch cells deliver reversible capacities of over 1200  $\text{mA h g}^{-1}$  at 0.01C, where the sulfur loadings were controlled to be 0.5 and 1.8  $\text{mg cm}^{-2}$ .<sup>37</sup> The aforementioned achievements indicate promising prototypes for high energy density SSLBs.

In summary, to realize practical SSLBs with thin SSEs, the methods listed in Section 2.1 may still not be enough. Thin SSEs should be endowed with different physical, chemical, and electrochemical properties to meet the requirements of individual SSLB systems and the detailed requirements and suitable SSE systems can be seen in Table S2 (ESI†). All SSLB systems

need good interfacial contact between SSE and electrode to reduce the interfacial resistance and battery impedance.<sup>108,109</sup> For example, a small amount of liquid electrolyte/ionic liquid or a thin layer of SPE is necessary to reduce the interfacial resistance and improve the electrochemical performance of thin oxide SSE-based SSLBs.<sup>44,45</sup> Cathode-supported SSEs are more desirable than free-standing SSE due to their better interface contact.<sup>36,54</sup> Additionally, melting Li is beneficial towards reducing the Li/SSE interfacial resistance.<sup>45,46</sup> Another important parameter for SSLBs is the ESW. Generally, a relatively low oxidation stability potential of 3 V is required by Li–S batteries; thus almost all kinds of SSEs can be used in this system. In this regard, most of the efforts are focused on solving the shuttling effect and interfacial issues.<sup>4</sup> In contrast, Li–LCO, Li–NMC, and Li–O<sub>2</sub> batteries have higher requirements on the ESW of SSEs. A higher oxidation stability potential of 4.3 V is needed to ensure high capacity output. Among the various SSEs, only some oxide and halide SSEs with oxidation stability limits of over 4.2 V can be directly used as the ionic conductors in cathode composites.<sup>8,15</sup> For SPE and sulfide SSEs, the active materials should be protected to prevent side reactions between cathode materials and SSEs under high voltages.<sup>27,93,110</sup> Moreover, extending the ESW of SPEs and

sulfide SSEs *via* structural design to match compatibility with high voltage cathode materials is another good direction.<sup>88,89</sup> Last but not least, rational electrode and battery structural design beyond SSEs also has a great effect on battery performance. With this in mind, to maximize the electrochemical performance of SSEs, both the anode and cathode should be properly designed. For instance, 3D Li structures can be used to prevent Li dendrite growth,<sup>39,40</sup> interconnected Li<sup>+</sup> transport channels built within the cathode may facilitate Li<sup>+</sup> transport,<sup>92</sup> and the introduction of electrocatalysts to enhance the electrochemical reaction kinetics should be beneficial to the overall SSLB performance.<sup>100,101</sup>

#### 2.4 Advanced characterization techniques for solid-state electrolyte and interface studies

As discussed above, the properties of SSEs and their compatibility with electrodes have a great influence on the electrochemical performance of SSLBs, including their ionic conductivity and interfacial transport kinetics. Understanding the Li<sup>+</sup> transport and interface evolution in depth is of significance for guiding the design of SSEs and their combination with electrodes in SSLBs. With this in mind, the development of advanced characterization techniques to reveal the buried mechanisms is urgently required. So far, some *ex* and *in situ* characterization techniques have been developed to identify the Li<sup>+</sup> transport pathway in SSEs as well as the structural evolution of SSEs at the SSE/electrode interface.<sup>111,112</sup> For instance, Cheng *et al.* reported that SSLBs using small particles of LLZO (1  $\mu\text{m}$ ) showed better electrochemical performance than those using large particles of LLZO (10  $\mu\text{m}$ ). To clarify the roles of grain orientations and grain boundary distributions in determining their electrochemical performance, high-resolution synchrotron polychromatic X-ray Laue microdiffraction was carried out to examine the differences between the two types of LLZO particles. As shown in Fig. 9A, the results suggested that there is a negligible difference in grain orientation between the two particle sizes and most of the grain orientations are randomly distributed. In other words, the grain orientation is not the determining factor towards the better electrochemical performance of SSLBs using small-grained LLZO. The electrochemical performance could be strongly affected by the microstructures and grain boundaries at the interfaces.<sup>113</sup>

Moreover, the Li<sup>+</sup> transport rate within the lattice and across the grain boundary also has a big effect on the ionic conductivity of SSEs and the electrochemical performance of SSLBs. Recently, nuclear magnetic resonance (NMR) was applied as a powerful tool for studying the Li<sup>+</sup> transport behavior. A good example is the study of the doping effect on the ionic conductivity of NaSICON-type electrolyte LATP. As shown in Fig. 9B, the effect of Al doping on ionic mobility in Li<sub>1+x</sub>Al<sub>x</sub>Ti<sub>2-x</sub>(PO<sub>4</sub>)<sub>3</sub> (with  $x = 0.0, 0.1, 0.2, 0.35, 0.5, 0.7$  and  $1.0$ ) was investigated by NMR to trace the structural changes. The temperature dependences of <sup>7</sup>Li NMR spin–lattice relaxation rates for the different compositions indicated that lower temperatures were required for  $x = 0.35$  and  $0.5$  to achieve a Li<sup>+</sup> ionic jump rate of  $\sim 4 \times 10^5 \text{ s}^{-1}$ . The results demonstrated that the optimal Al doping concentrations were  $0.35$  and  $0.5$ , where Li<sup>+</sup> exhibited maximum ionic mobility.<sup>114</sup> Apart from the Li<sup>+</sup>

transport rate within the SSE lattice, the total ionic conductivity of the SSE will be limited by the transport rate across the grain boundary, which has been considered the slowest step in long-range diffusion.<sup>61</sup> Lotsch *et al.* performed temperature-dependent pulsed field gradient (PFG) NMR spectroscopy to probe Li<sup>+</sup> diffusion processes at shorter and longer ranges in Li<sub>7</sub>SiPS<sub>8</sub> electrolyte. They found the presence of an amorphous thiophosphate side phase that hindered the intergrain conductivity, resulting in poor total ionic conductivity.<sup>115</sup> In another case, Wagemaker's group explored the Li<sup>+</sup> motion at the grain boundary between Li<sub>6</sub>PS<sub>5</sub>Br and Li<sub>6</sub>PS<sub>5</sub>Cl powders using two-dimensional <sup>6</sup>Li–<sup>6</sup>Li exchange NMR. As displayed in Fig. 9C, the <sup>6</sup>Li–<sup>6</sup>Li exchange spectra showed obvious Li shift from Li<sub>6</sub>PS<sub>5</sub>Br to Li<sub>6</sub>PS<sub>5</sub>Cl and *vice versa* within a mixing time of over 100 ms. The activation energy at the grain boundary was 0.27 eV, which is comparable to the value obtained in bulk Li<sub>6</sub>PS<sub>5</sub>Br and Li<sub>6</sub>PS<sub>5</sub>Cl SSEs ( $\sim 0.2$  eV). In other words, in the argyrodite SSE system, the Li<sup>+</sup> transport at the boundary is not the rate-limiting step.<sup>116</sup> The NMR “labeling” method makes it possible to attain the Li<sup>+</sup> movement behavior in the lattice or at the grain boundaries, which has the potential to be shifted to other SSE systems in the future.

Besides the effect of the Li<sup>+</sup> transport rate in the lattice and at the boundary, the ionic conductivity of SSEs is also related to the crystallinity. *In situ* X-ray diffraction (XRD) is a powerful tool for tracking the evolution of crystal structure during the synthesis process. For instance, Adams's group optimized the synthesis process of LAGP based on the analysis of *in situ* synchrotron XRD. As shown in Fig. 9D, the XRD results showed that the lowest crystallization temperature is 570 °C, while a higher heating temperature of over 730 °C is required to ensure the effect of Al doping into the LAGP structure, where obvious splitting of (214) and (300) peaks appeared in the XRD patterns. Additionally, the *in situ* XRD also provided a detailed phase change during Al doping. At the early stages of crystallization, Al-poor LGP is the dominant phase. When further heating the samples, the Al-poor LGP phase gradually disappeared, attributed to a more homogenous structure. In contrast, if heating the samples to higher temperatures of over 950 °C, the extraction of Al from the outer shell of LAGP particles was observed and followed by the formation of a germanium mullite impurity phase. The impurity phase decomposed into AlPO<sub>4</sub> upon cooling, which resulted in deviations of the Al-content in the final products. With this in mind, during LAGP synthesis, it is of significance to control the annealing temperature in the range of 730–950 °C to realize high-crystallinity pure phase LAGP.<sup>117</sup> Following this work, this technique has been shifted to other SSE systems (LLZO,  $\beta$ -Li<sub>3</sub>PS<sub>4</sub>) to study the phase evolution during the annealing process.<sup>118,119</sup> Recently, *in operando* XRD was also used to investigate the air- and humidity-stability of Li<sub>3</sub>InCl<sub>6</sub> by our group. The results showed that Li<sub>3</sub>InCl<sub>6</sub> presented high stability in dry-air, where the peaks belonging to Li<sub>3</sub>InCl<sub>6</sub> did not change during exposure to dry-air for over 24 h. In contrast, in the air with 30% humidity, the peaks belonging to Li<sub>3</sub>InCl<sub>6</sub> became weak and gradually disappeared after exposure for 10 min. Subsequently, a new set

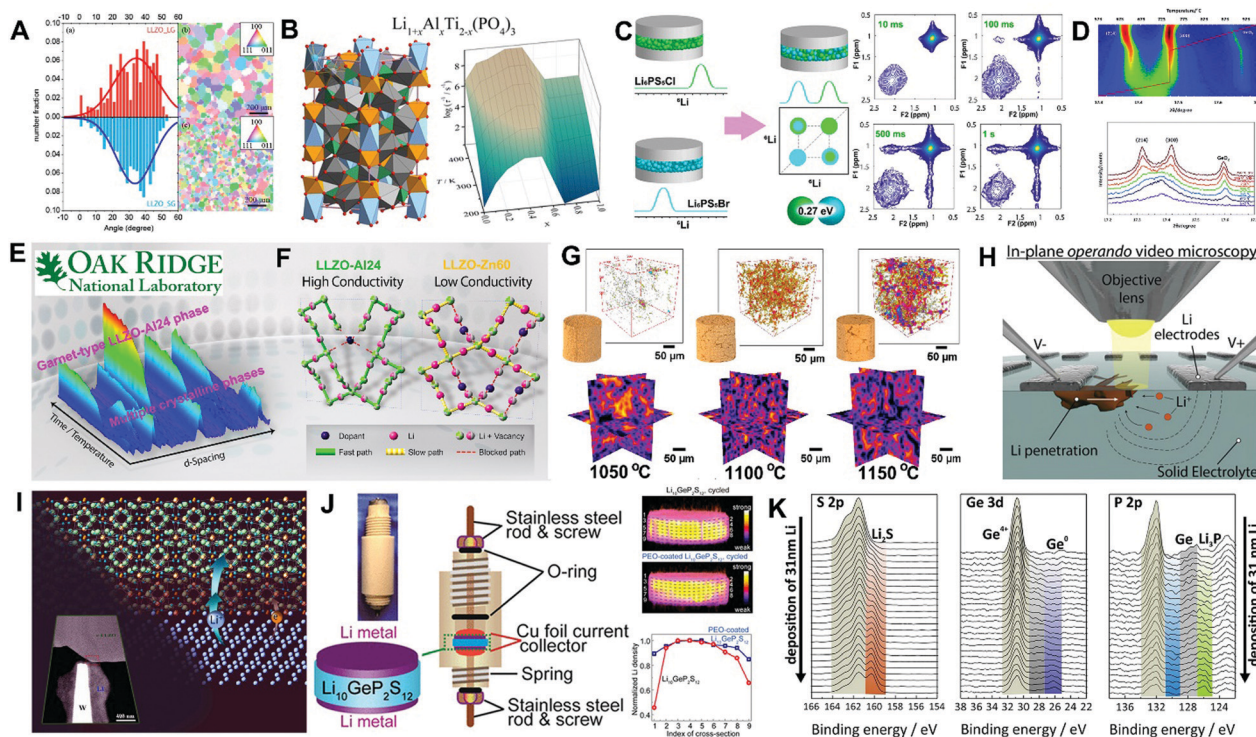


**Fig. 9** (A) Histograms of angles and grain orientation mappings of different LLZO particles. Reproduced with permission from ref. 113. Copyright (2015) American Chemical Society. (B)  $^7\text{Li}$  spin-lattice relaxation rates against the measurement temperatures for LATP samples with different amounts of Al doping. Reproduced with permission from ref. 114. Copyright (2016) American Chemical Society. (C) Schematic illustration of  $\text{Li}^+$  motion at the grain boundary and relative two-dimensional  $^6\text{Li}$ - $^6\text{Li}$  exchange spectra of mixtures of  $\text{Li}_6\text{PS}_5\text{Br}$  and  $\text{Li}_6\text{PS}_5\text{Cl}$  nanopowders with different mixing times. Reproduced with permission from ref. 116. Copyright (2019) American Chemical Society. (D) *In situ* XRD patterns of LAGP during the annealing process. Reproduced with permission from ref. 117. Copyright (2016) Royal Society of Chemistry. (E) Phase evolution during LLZO-Al24 garnet synthesis identified by *in situ* neutron diffraction. Reproduced with permission from Oak Ridge National Laboratory<sup>122</sup> and ref. 121. Copyright (2015) Royal Society of Chemistry. (F) The  $\text{Li}^+$  transport pathways in the models of high ionic conductivity LLZO-Al24 and low ionic conductivity LLZO-Zn60. Reproduced with permission from Oak Ridge National Laboratory<sup>122</sup> and ref. 123. Copyright (2015) American Chemical Society. (G) Pore-size color maps and distance maps for SSE microstructures sintered at different temperatures. Reproduced with permission from ref. 124. Copyright (2019) American Chemical Society. (H) Schematic illustration of *in situ* optical microscopy used to probe Li dendrite propagation in SSE. Reproduced with permission from ref. 131. Copyright (2020) Cell Press. (I) Structural evolution of LLZO at the interface revealed by scanning transmission electron microscopy coupled with electron energy loss spectroscopy (STEM-EELS). Reprinted with permission from ref. 132. Copyright 2016, American Chemical Society. (J) Schematic of and a real cylindrical cell for 3D MRI.  $^7\text{Li}$  3D MRI images and normalized  $^7\text{Li}$  densities of cycled LGPS pellets with and without PEO coating. Reprinted with permission from ref. 133. Copyright 2018, American Chemical Society. (K) XPS spectra recorded during the deposition of Li metal on LGPS. Reprinted with permission from ref. 134. Copyright 2016, American Chemical Society.

of peaks belonging to  $\text{Li}_3\text{InCl}_6 \cdot x\text{H}_2\text{O}$  and  $\text{LiCl}$  appeared, indicating the occurrence of side-reactions. Based on the XRD results, it is believed that  $\text{Li}_3\text{InCl}_6$  is a dry air-stable SSE, and its humidity-stability should be further improved. This conclusion was further consolidated by *in situ* Raman and *in situ* X-ray absorption near-edge structure (XANES).<sup>120</sup>

As we mentioned in the Introduction, elemental doping is an effective strategy to improve the ionic conductivities of SSEs. To deeply understand the roles of dopants during the synthesis process, *in situ* neutron diffraction allows for a direct observation of the doping effects by monitoring the phase evolutions. An and his-coworkers from Oak Ridge National Laboratory found that a phase evolution to low-conductivity tetragonal phase occurred during the cooling process at around 630 °C for LLZO synthesis, resulting in low ionic conductivity. With the introduction of Al dopant, the high-conductivity cubic phase (named LLZO-Al24) could be stabilized and the formation of

the low-conductivity phases was suppressed (Fig. 9E). However, small amounts of intermediate phases (*e.g.*  $\text{LaAlO}_3$ ,  $\text{LiAlO}_2$ ) and a low-conductivity tetragonal phase were detected in the as-synthesized bulk. The intermediate phases can be attributed to the liquid  $\text{Li}_2\text{CO}_3$  evaporation that results in non-stoichiometric composition, while the residual tetragonal phase forms because of diffusion processes.<sup>121,122</sup> It is a widely adopted concept that creating more Li vacancies is beneficial for increasing the ionic conductivity. For instance, in An's work, both Al and Zn doped LLZO SSEs (labeled LLZO-Al24 and LLZO-Zn60) showed positive effect in increasing Li vacancy concentration. However, LLZO-Al24 delivered a high ionic conductivity of  $10^{-4} \text{ S cm}^{-1}$ , while LLZO-Zn60 only showed a low ionic conductivity of  $10^{-7} \text{ S cm}^{-1}$ . To reveal the relationship between Li vacancies and ionic conductivity with different elemental doping, neutron diffraction was further applied to identify the Li state in the doped LLZO SSEs. As illustrated in Fig. 9F, in the

LLZO-Al<sub>24</sub> system, a number of vacancies were observed in the active octahedral sites, which bridged the two neighboring tetrahedral sites and enabled a fast Li<sup>+</sup> pathway. The fast pathways throughout the garnet 3D framework were attributed to the high conductivity of LLZO-Al<sub>24</sub>. In contrast, in LLZO-Zn<sub>60</sub>, nearly all the vacancies were located at the inactive octahedral sites and lacked vacancies in the active sites. The fully occupied octahedral sites supplied less opportunity for Li<sup>+</sup> hopping and led to a slow transport pathway.<sup>122,123</sup> Based on the neutron diffraction results, we believe that the ionic conductivity of SSEs has the potential to be further improved by exploring new doping elements to further reduce the residual tetragonal and intermediate phases while increasing vacancies in active octahedral sites.

Apart from the aforementioned factors, the porosity and tortuosity of SSEs also have significant effects on the ion-transport behavior in 3D SSE structures. Accurate 3D reconstruction with fine microstructure resolution obtained by X-ray computed tomography (CT) can be used to experimentally observe the continuous ionic transport paths in SSEs. Hatzell's group investigated the tortuosity of LLZO with different sintering temperatures from 1050 °C to 1150 °C based on X-ray CT. As shown in Fig. 9G, they found that the electrolyte tortuosity and the tortuosity directional anisotropy gradually increased with increasing sintering temperature.<sup>124</sup> The high tortuosity and large grain boundaries in SSEs promote Li dendrite growth and propagation, resulting in low critical current densities (CCD). The LLZO SSE annealed at 1050 °C could tolerate a current density of 0.025 mA cm<sup>-2</sup>, while a short-circuit was observed at 0.013 mA cm<sup>-2</sup> for the LLZO obtained at 1100 °C and 1150 °C.<sup>125</sup> To promote the utilization of SSEs in practical application, the mechanical properties are another important consideration. The mechanical strength of SSEs plays an important role in suppressing the growth of lithium dendrites, increasing the interfacial stability and even avoiding the propagation of cracks.<sup>126</sup> Young's modulus has been recognized as one of the most significant tools for evaluating the mechanical strength of SSEs. For instance, oxide- and sulfide SSEs possess Young's moduli of 90–155 GPa/8–30 GPa, respectively, which are strong enough to suppress Li dendrite growth in principle.<sup>126</sup> Nevertheless, the short-circuit phenomenon is a common issue in SSLBs based on oxide- and sulfide-SSEs. The grain boundaries and voids in the bulk SSEs deteriorate the mechanical strength and Li dendrite suppression capability. One of the most promising strategies is to reduce the voids and increase the tap density of SSEs, which has been demonstrated to be effective in increasing the mechanical properties and Li dendrite suppression as well as reducing the interfacial resistance.<sup>127,128</sup> To identify the role of voids in Li dendrite growth and deterioration of SSE performance, X-ray CT was applied to observe the Li dendrite growth process in β-Li<sub>3</sub>PS<sub>4</sub> electrolyte. During the Li plating/stripping process, the highly mobile Li atoms were forced into the void spaces within the SSE. Once the void space was occupied, continued Li growth could damage the β-Li<sub>3</sub>PS<sub>4</sub> grains, resulting in structural deformation and battery failure.<sup>129</sup> These results further emphasize the importance of developing high-density SSEs and minimizing the grain

boundary resistance. In another case, X-ray CT was applied to image interphase growth and its effect on the mechanical degradation of LAGP. The results showed that the interphase growth accompanied by volume expansion forced large crack formation in LAGP. The formation of large cracks is the root cause of an increase in Li<sup>+</sup> transport resistance and the chemomechanical degradation of the SSE layer.<sup>130</sup>

To achieve high-performance SSLBs, the interface information at the SSE/electrode interface beyond the intrinsic properties of SSEs should be further clarified. *In situ* optical microscopy (OM) and scanning transmission electron microscopy coupled with electron energy loss spectroscopy (STEM-EELS) were developed to probe the structural evolution of the Li-LLZO interface.<sup>131,132</sup> As shown in Fig. 9H, Dasgupta *et al.* detected multiple Li morphologies (straight, branching, spalling, and diffuse) penetrating the SSE by *in situ* OM, demonstrating that Li propagation is a complex process. Moreover, they found that the different Li morphologies are recyclable during the plating/stripping process. At high current densities, the mechanical cracking of SSE is the most common cause of Li filament propagation, and the propagation rate is proportional to the current density. Additionally, the unstable Li stripping at high current densities results in void formation and increased contact resistance, which was considered to be the reason for the increased overpotential. In other words, both the Li plating and stripping processes should be taken into careful consideration during the rational Li/SSE interface design.<sup>131</sup> In another case, as shown in Fig. 9I, Chi's group developed *in situ* STEM-EELS equipment to study the interfacial stability of the Li/LLZO interface. Upon contact with Li metal, the reduction reaction of LLZO was observed followed by the formation of a tetragonal-like LLZO interface with a thickness of about 5 unit cells. Such a thin interface has a negligible influence on the ionic conductivity of bulk LLZO but can inhibit further interfacial reactions between Li and LLZO. This work provided new insight into the reactivity of the Li/SSE interface.<sup>132</sup>

Besides Li dendrite growth in SSEs, the unstable Li/SSE interface is another challenge that has hindered the practical application of SSLBs. In this regard, understanding the interfacial reactions between Li and SSE in detail is of significance in paving the way for high-performance SSLBs. Very recently, 3D <sup>7</sup>Li magnetic resonance imaging (MRI) was developed to evaluate Li distribution homogeneity at the Li/LGPS interface within Li-Li symmetric cells. As shown in Fig. 9J, the 3D <sup>7</sup>Li MRI images demonstrated that a large amount of Li was consumed at the Li/LGPS interface, attributed to the heterogeneous Li distribution during cycling. The formation of Li deficiency at the Li/LGPS interface was considered to be the main reason for the continuous increase of interfacial resistance. The situation of significant Li consumption at the interface could be alleviated by the introduction of a PEO/LiTFSI SPE to stabilize the interface.<sup>133</sup> This work proved that 3D <sup>7</sup>Li MRI is a powerful tool for monitoring the Li distribution at the interface. The unstable Li/LGPS system was further clarified by Janek's group. The *in situ* X-ray photoelectron spectroscopy (XPS) spectra in Fig. 9K display the decomposition products of LGPS

(Li<sub>2</sub>S, Ge and Li<sub>3</sub>P), indicating the instability of LGPS to Li. This finding coincides well with the 3D <sup>7</sup>Li MRI result and can be used to explain the consumption of Li at the Li/LGPS interface.<sup>134</sup> A similar decomposition reaction of SSEs at the Li/SSE interface was also detected in other SSE systems such as LLTO and Li<sub>2</sub>S–P<sub>2</sub>S<sub>5</sub> by *in situ* XPS. Reduced Ti species (Ti<sup>3+</sup>, Ti<sup>2+</sup> and Ti metal) were detected at the Li/LLTO interface during cycling, indicating the electrochemical instability of LLTO to Li.<sup>135</sup> In another case, Teeter and his coworkers studied the effect of oxygen contaminations on Li<sup>+</sup> transport at the Li/Li<sub>2</sub>S–P<sub>2</sub>S<sub>5</sub> interface. The oxygen contaminants can react with Li<sub>2</sub>S–P<sub>2</sub>S<sub>5</sub> and initially result in Li<sub>3</sub>PO<sub>4</sub> phase segregation and subsequent Li<sub>2</sub>O formation. Li<sub>3</sub>PO<sub>4</sub> exhibited the largest overpotential, which was considered to be the determining factor leading to irregular Li deposition and deterioration of the battery performance.<sup>136</sup>

In summary, advanced *ex situ* and *in situ* characterization techniques play very important roles in understanding the Li<sup>+</sup> transport mechanisms in SSEs as well as the structural evolutions of SSEs at the interface. These characterization techniques are beneficial for revealing the underlying mechanism behind the limited ionic conductivity and interface instability, thus providing guidelines for designing higher ionic conductivity SSEs and more favorable interfaces for SSLBs. More efforts should be devoted towards developing advanced characterization techniques for anodes, cathodes, and SSEs and their interfaces concurrently. Due to the limited information obtained from any single characterization technique, we strongly recommend the combination of multiple *in situ* characterization techniques to provide a more comprehensive understanding to aid in the development of high-performance SSLBs.

## 2.5 Energy density evaluation for thin SSLBs

As previously mentioned, thin SSEs are critical for achieving SSLBs with high energy density. In practical application, the energy density, including gravimetric energy density and volumetric energy density, should be evaluated based on the cell-level packaging rather than just a rough estimation from cathode/anode active materials. In a typical cell, the components that contribute to weight (or volume) include active and non-active materials in both the cathode and anode, electrolyte, current collectors, tabs and packaging materials. With this in mind, there is a significant difference between the package weight and active material weight, resulting in a large gap between practical energy density and theoretical values based on active materials alone.

Considering the fact that the development of SSLOBs is still in a state of infancy and the open system requires drastically different cell configurations compared to other systems (Li-ion, Li–S batteries), we chose to simulate the gravimetric/volumetric energy densities of SSLBs with 5 common cathode materials (LFP, LCO, NMC-811, Li-rich and S), where metallic Li was chosen as the anode material. To evaluate the effect of different SSEs, three typical SSEs, including LGPS (sulfide, 2.05 g cm<sup>-3</sup>), LLZO (oxide, 5.10 g cm<sup>-3</sup>), and PEO (polymer, 1.24 g cm<sup>-3</sup>) were chosen for simulation. Detailed parameters of the selected

electrodes and SSE systems are listed in Table S3 (ESI<sup>†</sup>). The parameters in Table S3 (ESI<sup>†</sup>) for Li–LFP, Li–LCO, Li–NMC-811 and Li–Li-rich SSLBs are calculated based on the method reported in Chen's review paper,<sup>29</sup> while the parameters for the Li–S system are according to our previous reports.<sup>3,4</sup> The areal capacities of the LFP, LCO, NMC-811 and Li-rich cathodes are controlled to be 4 mA h cm<sup>-2</sup> for the energy density calculations, corresponding to active material loadings of 23.53, 21.05, 19.05 and 13.33 mg cm<sup>-2</sup>. For Li–S batteries, the areal capacity is controlled to be 6 mA h cm<sup>-2</sup>, equaling to a sulfur loading of 4.49 mg cm<sup>-2</sup> based on 80% sulfur utilization (1338 mA h g<sup>-1</sup>). The gravimetric and volumetric energy densities of the SSLBs are calculated based on a pouch cell format, where the pouch cells are assembled by repeatedly laminating the anode, SSE and cathode layers. In this review, the configuration of the pouch cells includes 22-layers of a double sided cathode, similar to Chen's review paper.<sup>29</sup> A 16 μm Al foil and an 8 μm Cu foil are chosen as the cathode and anode current collectors, respectively. The size of the pouch cell is fixed at 138 mm × 81.8 mm × thickness (mm) (including package (152 μm for each layer)). Considering that the weights/thicknesses of the anode, cathode and sealing package are fixed, the total weight/thickness of the pouch cell will vary depending on the SSE weight/thickness. Table S4 (ESI<sup>†</sup>) lists the detailed cell parameters used for constructing a Li–LCO pouch cell with a gravimetric/volumetric energy density of 365.0 W h kg<sup>-1</sup>/784.5 W h L<sup>-1</sup> based on a 30 μm LGPS SSE layer.

The effect of SSE thickness on the gravimetric/volumetric energy densities in different SSLB systems is shown in Fig. 10A–I. The thickness of the SSE layer varies from 5 μm to 100 μm. For the calculations, the contents of LFP, LCO, NMC-811 and Li-rich active materials in the cathodes are set at 80 wt%, 85 wt% and 90 wt%. Considering the poor electron transport in sulfur cathodes, additional conductive carbon is required in the cathode mixture and the sulfur content is set at 50 wt%, 60 wt% and 70 wt%. The areal capacity ratio of the negative to positive electrodes (N/P ratio) is set at 2. Among the five SSLB systems, the Li–S batteries show the highest gravimetric energy density due to their high discharge capacity. They can achieve high gravimetric energy densities of over 500 W h kg<sup>-1</sup>/450 W h kg<sup>-1</sup> when the thickness of the PEO/LGPS layer is controlled to be less than 30 μm. Even when further increasing the thickness of PEO/LGPS to 100 μm, high energy densities of around 288 (50 wt% S, LGPS) to 389 W h kg<sup>-1</sup> (70 wt% S, PEO) can be achieved. In contrast, when replacing the PEO/LGPS SSEs with LLZO, which has a much higher density (5.10 g cm<sup>-3</sup>), the gravimetric energy density of the Li–S cells will decrease to 340 W h kg<sup>-1</sup> and 160 W h kg<sup>-1</sup> for electrolyte layers of 30 μm and 100 μm thicknesses, respectively. Besides, the Li-rich material as a representative of a high-capacity cathode material in Li-ion batteries enables SSLBs with high energy densities comparable with Li–S batteries. Generally, they can achieve high energy densities over 450 W h kg<sup>-1</sup> when the thickness of the PEO/LGPS layer is controlled to be less than 30 μm and the active material content in the cathode is higher than 85 wt%. When using LLZO as the SSE, a thickness of lower than 20 μm is

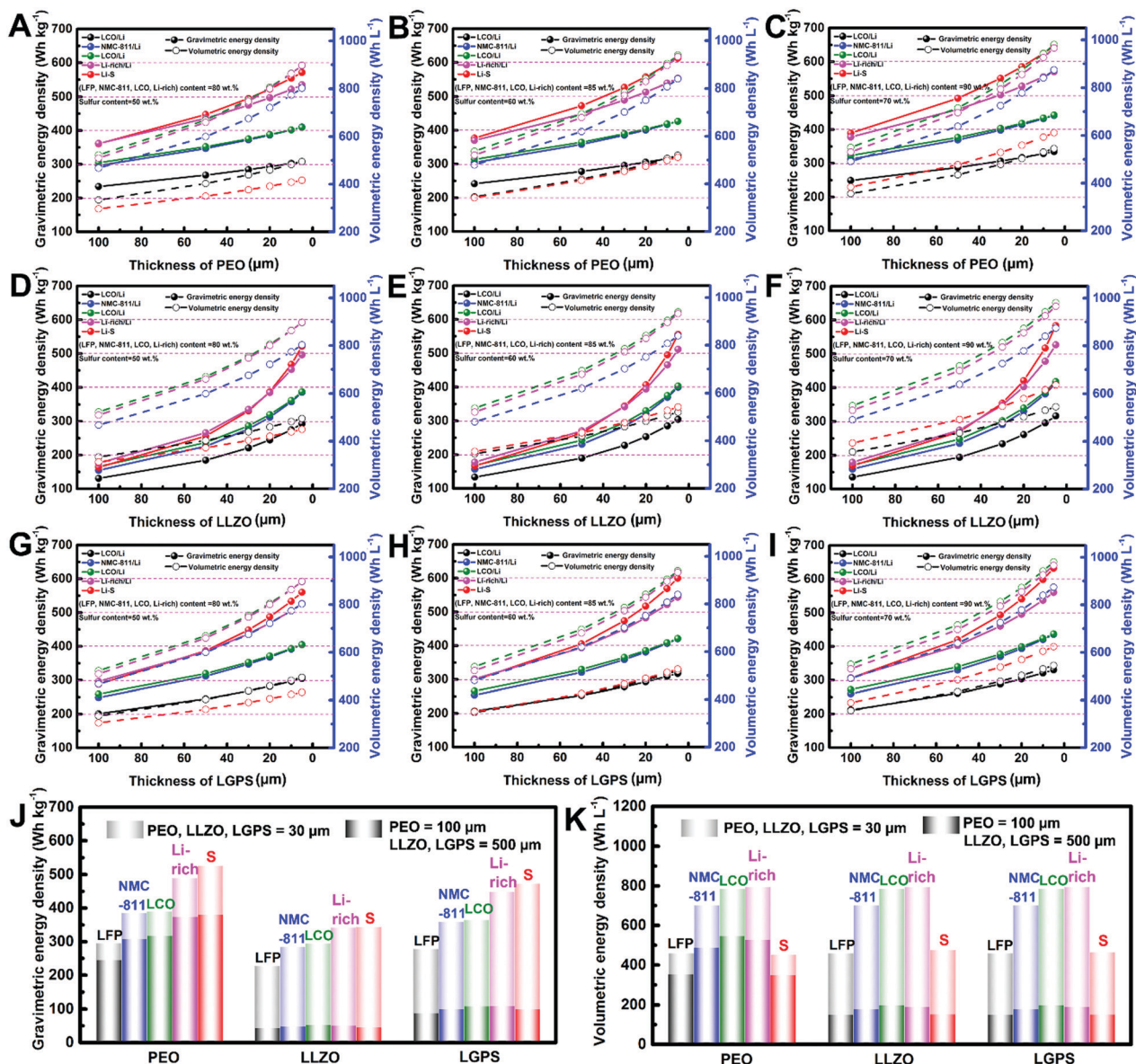


Fig. 10 Gravimetric and volumetric energy densities of SSLBs as functions of SSE thickness. (A–C) PEO, (D–F) LLZO, and (G–I) LGPS. The LFP, LCO, NMC-811, Li-rich and S contents in the cathodes are (A, D and G) 80 wt%, 80 wt%, 80 wt%, 80 wt%, and 50 wt%; (B, E and H) 85 wt%, 85 wt%, 85 wt%, 85 wt%, and 60 wt%; and (C, F and I) 90 wt%, 90 wt%, 90 wt%, 90 wt%, and 70 wt%. (J) Gravimetric energy densities and (K) volumetric energy densities of SSLBs based on target SSEs (PEO, LLZO, LGPS = 30 μm) and widely reported SSEs (PEO = 100 μm, LLZO, LGPS = 500 μm). The active material contents are 85 wt% for the LFP, LCO, NMC-811 and Li-rich cathodes and 60 wt% for the S cathode.

essential to achieve a high energy density of over  $400 \text{ W h kg}^{-1}$ . It should be mentioned that the capacity for Li–Li-rich SSLBs we set here is only  $4 \text{ mA h cm}^{-2}$ , corresponding to an active material loading of  $13.3 \text{ mg cm}^{-2}$ . There is still large room for further improvement of the energy density, even over  $500 \text{ W h kg}^{-1}$ . Among all four SSLB systems, Li–LCO and Li–NMC-811 present similar energy densities regardless of the set parameters. To realize an energy density of over  $300 \text{ W h kg}^{-1}$ , the thickness of the PEO, LGPS and LLZO SSEs should be no more than 100, 50 and 30 μm, respectively. Moreover, if the thickness of PEO can be controlled to be less than 30 μm and the LCO/NMC-811 content up to 90 wt%, the Li–LCO/NMC-811 has the potential to realize an

energy density of over  $400 \text{ W h kg}^{-1}$ . One point that should be mentioned is that the LCO and Li-rich materials chosen here are high-voltage materials. A high charging voltage of greater than 4.5 V is needed to ensure the capacity output (LCO:  $190 \text{ mA h g}^{-1}$ ; Li-rich:  $300 \text{ mA h g}^{-1}$ ). Nevertheless, the use of high-voltage LCO and Li-rich puts forward more stringent limitations on the electrochemical stability of both the cathode material and SSEs under high voltages. With this in mind, Li–NMC-811 may be a more suitable system in the near future. Among the four SSLB systems, Li–LFP displays the lowest energy densities. Even with a low SSE thickness of 30 μm, a high energy density of over  $300 \text{ W h kg}^{-1}$  can only be achieved by combining PEO electrolyte

and 90 wt% active material content. However, due to the nano-sized LFP particles which has a higher specific surface area, a higher SSE content is required to maintain interconnected  $\text{Li}^+$  transport pathways. Moreover, it is difficult to ensure high capacity output with an active material content of 90 wt%. In other words, the Li-LFP SSLB is not a suitable system for high energy density cell designs.

Besides the gravimetric energy density, the volumetric energy density is another important parameter to evaluate for practical SSLB application. As shown in Fig. 10A-I, the Li-LCO and Li-Li-rich SSLBs present the highest volumetric energies. In the fixed SSLB system, the volumetric energy density is affected by the thickness of SSE and active material contents, while the SSE type has a negligible impact. According to our simulations, the Li-LCO and Li-Li-rich SSLBs can deliver high volumetric energy densities of over  $500 \text{ W h L}^{-1}$  with the parameters provided in Fig. 10A-I. If the SSE thickness is  $30 \mu\text{m}$ , higher energy densities in the range of roughly  $750 \text{ W h L}^{-1}$  (80 wt% LCO or Li-rich) to  $810 \text{ W h L}^{-1}$  (90 wt% LCO or Li-rich) can be achieved. As mentioned above, the LCO and Li-rich chosen here are high-voltage cathode materials, which are unlikely to be realized in SSLBs in the near future. With this in mind, we further calculated the volumetric energy densities of the Li-NMC-811 SSLBs. The volumetric energy densities of the Li-NMC-811 SSLBs are a bit lower than those of the Li-LCO and Li-Li-rich SSLBs with the same parameters. Nevertheless, with a SSE thickness of  $30 \mu\text{m}$ , high volumetric energy densities in the range of  $675 \text{ W h L}^{-1}$  (80 wt% NMC-811) to  $725 \text{ W h L}^{-1}$  (90 wt% NMC-811) can be achieved. Among the four SSLB systems, Li-S and Li-LFP show the lowest volumetric energy densities due to the nano-sized active materials and the low density of the cathode composite. It is very difficult to achieve a high volumetric energy density of over  $500 \text{ W h L}^{-1}$  when the thickness of the SSE is greater than  $50 \mu\text{m}$ .

To understand the gap between the energy density goals ( $300 \text{ W h kg}^{-1}$  and  $500 \text{ W h L}^{-1}$ ) and the current state of research more intuitively, the gravimetric and volumetric energy densities of the aforementioned SSLB systems with a  $30 \mu\text{m}$  SSE compared to some of the most widely reported SSEs (PEO:  $100 \mu\text{m}$ , LGPS/LLZO:  $500 \mu\text{m}$ ) are listed in Fig. 10J and K respectively. The active material contents of the cathodes are 85 wt% for LFP, LCO, NMC-811 and Li-rich and 60 wt% for S. For the polymer electrolytes, the widely reported thicknesses are around  $100 \mu\text{m}$ , which enable the Li-LFP, Li-LCO, Li-NMC-811, Li-Li-rich and Li-S SSLBs with gravimetric energy densities of 242, 304, 314, 370 and  $377 \text{ W h kg}^{-1}$ . Moreover, the relevant volumetric energy densities are 345, 479, 537, 520 and  $342 \text{ W h L}^{-1}$ , respectively. In other words, if we ignore the electrochemical performance and practical issues of PEO electrolyte, the recently reported PEO electrolyte in the literature can almost meet the requirements of both high gravimetric energy density and volumetric energy density in Li-Li-rich, Li-NMC-811 and Li-LCO systems. In contrast, in most cases, the reported oxide- and sulfide-SSEs in SSLBs are over  $500 \mu\text{m}$ . According to our simulations, the gravimetric energy densities are in the range of  $40\text{--}104 \text{ W h kg}^{-1}$ , while the volumetric energy densities are in the range of  $143\text{--}191 \text{ W h L}^{-1}$ ,

which are significantly lower than the desired energy density goals. In this regard, we can conclude that thin SSEs are of significance for pursuing high energy density SSLBs. For polymer electrolyte, we should be focused on enhancing the electrochemical performance of SSLBs, such as extending the ESW to match the high-voltage cathodes, and enhancing the Li dendrite suppression capability of the electrolyte layer. For ceramic SSEs, more effort should be devoted towards developing thin SSEs with thicknesses less than  $30 \mu\text{m}$ .

### 3. Conclusions and perspectives

The pursuit of high safety and high energy density has accelerated the development of thin SSE-based SSLBs, especially for EV applications. As illustrated in Fig. 11, compared with thick SSEs, thin SSEs reduce the inactive material content and the thickness of the pouch cells, thus improving the gravimetric/volumetric energy density. Moreover, thin SSEs reduce internal resistance, which is beneficial towards enhancing the rate performance and power density. Additionally, the cost of SSLBs can be reduced with thin layered SSEs, which is of significance for promoting their commercialization. In this review, we summarized the recent progress in thin layered SSE fabrication. The rational structural/functional design of thin SSEs and their application in different SSLB systems, including coin cells, model cells and pouch cells, were introduced. Moreover, the underlying  $\text{Li}^+$  transport rules and the evolution of the SSE/electrode interface were clarified *via ex* and *in situ* advanced characterization techniques. Additionally, the gravimetric and volumetric energy densities of SSLBs as functions of SSE thickness with three types of SSEs (polymer, oxide and sulfide SSEs) were evaluated. Through analysis of the battery components, the target thicknesses of SSEs required to achieve practical gravimetric/volumetric energy densities over  $300 \text{ W h kg}^{-1}/500 \text{ W h L}^{-1}$  were clarified. Although promising results have been achieved using thin SSEs in SSLBs, there are still significant challenges

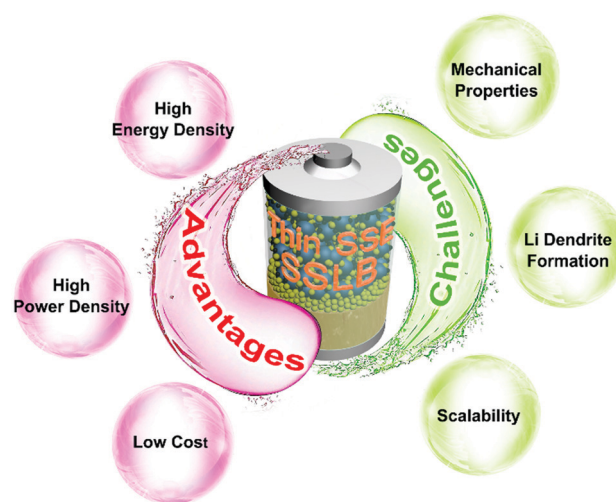


Fig. 11 Summary of the advantages and challenges of thin SSE-based SSLBs.

(in terms of mechanical strength, Li dendrite suppression, scalability, *etc.*) that need to be overcome. The potential directions and outlook for SSLBs can be summarized as follows.

### (1) The development of efficient fabrication strategies for thin SSEs

Further effort is required to develop simple and scalable fabrication methods for thin SSEs that can be used for industrial applications. As we mentioned in Section 2.1, many methods such as solution/slurry casting, hot pressing, solution infusion, extrusion and 3D printing have been developed for thin SSE fabrication. Among these methods, solution casting has already been demonstrated to be an effective, simple and scalable strategy to develop thin SPEs with thicknesses less than 100  $\mu\text{m}$ .<sup>36,106</sup> However, for ceramic SSEs, it remains challenging to fabricate large sheets of thin SSEs. For instance, as listed in Table S1 (ESI<sup>†</sup>), tape casting is the most widely adopted method for oxide-SSE fabrication and several reports have proved its potential for scalability.<sup>41,44,46</sup> Nevertheless, there have yet to be reports on free-standing oxide SSEs over 10  $\text{cm}^{-2}$  after annealing. Moreover, the brittleness of oxide SSEs, especially for thin SSEs, is another problem for battery manufacturing. Thin SSEs have been prepared using a slurry coating method, which is the most popular method for sulfide SSE fabrication. During slurry preparation, the choice of suitable solvent and binder is critical for electrolyte compatibility and mechanical properties. Moreover, the appropriate proportion of binder in the slurry is also important. The SSE particles will have poor interconnectivity if the binder proportion is too small. On the other hand, a high binder proportion will lead to discontinuous  $\text{Li}^+$  transport pathways and poor ionic conductivity.<sup>37,93</sup> The dry film method should be a very important direction in the future though it hasn't been used for thin SSE fabrication. It has already demonstrated its ability in the fabrication of large-size cathodes with thicknesses less than 100  $\mu\text{m}$ .<sup>23,137</sup> It is also worth mentioning that it is a solvent-free process and the binder content can be controlled as less than 0.1 wt%, which is of significance for producing large size SSE sheets with the well-maintained intrinsic ionic conductivity of SSEs. Equally important, a suitable transfer technique should be developed simultaneously to transfer the SSEs from the substrate to the surfaces of the electrodes. Despite the positive effect of reduced SSE thickness on improving both energy density and power density, the safety concerns associated with worsened mechanical strength should be taken into consideration. Thin SSEs should be endowed with strong mechanical strength to prevent electrode material penetration during battery assembly, especially under high-pressure to ensure good contact between electrodes and electrolyte. For the practical application of SSLBs, a single SSE may not meet all the requirements in terms of flexibility, Young's modulus, interfacial compatibility, ESW, ionic conductivity, *etc.* To compromise the drawbacks of single-component SSEs, the rational design of hybrid SSEs by combining two or more SSEs to balance the properties of each component may be a good solution. For instance, the introduction of SPEs can enhance the flexibility as well as solve the interface issues, while

ceramic SSEs are able to improve the ionic conductivity and mechanical strength to some extent. Additionally, most of the SPEs are stable to the Li anode, while oxide and halide SSEs show higher oxidation potentials. Their combination is expected to extend the ESW of composite SSEs and enables their successful application in high-voltage SSLB systems.

### (2) Improving the compatibility between thin SSEs and anodes/cathodes

According to the simulation results presented in Section 2.5, in order to achieve an energy density of 300  $\text{Wh kg}^{-1}$ /500  $\text{Wh L}^{-1}$ , thin SSEs should couple with high areal capacity cathodes (*e.g.* LFP, LCO and NMC8-11; Li-rich: 4  $\text{mAh cm}^{-2}$ , S: 6  $\text{mAh cm}^{-2}$ ). The thickness change of the electroactive Li during plating/stripping is in the range of 20–30  $\mu\text{m}$ . Moreover, consideration of the volume change of the cathode should not be neglected, especially for sulfur (80 vol%). Whether the mechanical strength of thin SSEs can tolerate the volume change during cycling should be further explored. To solve the issues with electrode volume fluctuation, several potential solutions are suggested. (1) The positive effect of externally applied pressure in improving the cycling performance should be considered, and smart package designs with applied pressure on pouch cells may be beneficial.<sup>138,139</sup> (2) Electrode design with void space for volume expansion. (3) Balancing the net volume change between two cathode materials with opposite volume expansion trends. For instance, Janek's group successfully combined LCO and NMC-811 to achieve an electrode with less overall volume fluctuation, where the volume contraction of NCM-811 was compensated for by the volume expansion of LCO during delithiation.<sup>140</sup> (4) Introduction of flexible components into thin SSEs to enhance their flexibility, thus improving their ability to tolerate volume change during cycling. Besides energy density, power density is equally important in practical application. Reducing the tortuosity of  $\text{Li}^+/\text{e}^-$  transport pathways and building continuous  $\text{Li}^+/\text{e}^-$  pathways are effective strategies. For instance, increasing the ratio of  $\text{Li}^+$  to  $\text{e}^-$  conductors in the electrode can help improve power density. Another effective strategy is to develop 3D continuous  $\text{Li}^+$  transport pathways in both anodes and cathodes to facilitate  $\text{Li}^+$  transport in the electrode (a vertically-aligned structure is more suitable).<sup>141–144</sup> Nevertheless, both of the strategies will require sacrifice of some energy density. In this regard, the energy density and power density should be balanced for practical application.

It is well known that one of the biggest advantages of SSLBs over traditional LIBs is their potential for high energy density when coupled with a Li anode. However, Li dendrite growth is still a critical bottleneck for the development of SSLBs, especially at high operating current densities and high capacities.<sup>145,146</sup> The situation will be more serious in thin SSE-based SSLB systems where Li dendrites have a shorter penetration depth before short-circuit. Using graphite and Li-metal alloys instead of Li metal has been proven to be an effective method to prolong the cycling life of SSLBs.<sup>40,93,107</sup> However, the higher potential of Li-metal alloys *vs.*  $\text{Li}^+/\text{Li}$  (*e.g.* Li–In:  $\sim 0.6$  V) and the low capacity output of graphite will

reduce the practical energy density. The application of a thin graphite or Li-metal alloy layer on the surface of the Li anode to maximize energy density and minimize voltage loss is worth further investigation.<sup>147,148</sup> Moreover, high-efficiency anode-free SSLBs have the potential to realize high energy density cell configurations.<sup>23,149</sup> Additionally, the development of effective Li protection methods is critical towards achieving stable and long-term electrochemical cycling of SSLBs.<sup>4,145</sup> Last but not least, according to Wang's report, the high electronic conductivity of SSEs is mostly responsible for dendrite formation. Lowering the electronic conductivity is therefore critical for suppressing Li dendrite formation and paving the way for the success of SSLBs.<sup>150</sup>

The ESW of SSEs is another consideration and should match the anode and cathode in different SSLB systems. For oxide- and halide-based SSEs, in most cases, their oxidization stability potentials are over 4.2 V, which can meet the requirements of high-voltage SSLBs.<sup>15,17,89</sup> According to Mo's simulation, F-based halide SSEs will have oxidization potentials greater than 6 V.<sup>16</sup> Nevertheless, their stability towards the Li anode is a big challenge due to the existence of high-valence metal-ions (e.g. LATP,  $\text{Li}_3\text{InCl}_6$ ). The formation of a mixed electronically-conductive interface will lead to the continuous decomposition of SSEs and increase of interfacial resistance. The introduction of buffer layers to limit the direct contact of SSE and the Li anode is one proposed direction, where the buffer layer should have reasonable thickness and relatively high ionic conductivity to reduce the  $\text{Li}^+$  transport resistance at the interfaces.<sup>151</sup> When the buffer layer is another type of SSE, such as SPES,  $\text{Li}_3\text{PS}_4$  or  $\text{Li}_6\text{PS}_5\text{Cl}$ , the structure is referred to as a double-layer SSE.<sup>14,152</sup> The buffer layer SSE is beneficial for inhibiting side reactions, while oxide- or halide-SSEs help suppress Li dendrite formation to some extent. To reduce the effect of the buffer layer on lowering the energy density, thin buffer layers are required. Methods such as physical vapor deposition and atomic layer deposition that are used to fabricate SSEs in the nano-scale are promising, leading to the maintenance of the high ionic conductivity of SSEs as well as high energy density.<sup>5,153</sup> Moreover, the replacement of high-valence metal-ions (e.g.  $\text{In}^{3+}$ ,  $\text{Ti}^{4+}$ ) and halogen elements (e.g. Cl, Br) with low-valence metal-ions (e.g.  $\text{Mg}^{2+}$ ) and F may be another promising direction to extend the reduction stability potential.<sup>16</sup> Of course, the ionic conductivity and reduction stability potential should be carefully balanced in this direction. SPES (typically PEO-based SPES) and metal-free sulfide-SSEs can be considered as Li anode stable SSEs through either the formation of a stable SEI or no side reactions. Furthermore, the oxidization stability response to high voltages is also challenging. Introducing inorganic fillers, changing functional groups, and adding another high-voltage-stable SSE layer to the cathode are effective methods to extend the oxidization stability windows of SPES.<sup>32,88,90</sup> Another potential direction is the combination of oxidization-tolerant polymers with high-ionic-conductivity inorganic SSEs, which can lead to composite SSEs with both high ionic conductivity and high oxidization stability.<sup>154</sup> For sulfide SSEs, the best way to realize their utilization in high-voltage SSLB

systems is to inhibit the direct contact between SSEs and cathode materials *via* coating methods due to their poor oxidation stability.<sup>27,155</sup>

For practical application, it is imperative to design thin SSEs that are compatible with both anodes and cathodes. For instance, SPE-based SSEs (e.g. PEO) show high solubility of polysulfides. Introducing some oxide SSEs as fillers is a strategy to that can limit polysulfide shuttling. On the other hand, oxide SSEs shows poor interfacial compatibility with cathodes/anodes, which can be solved by introducing a thin layer of SPE at the interface. Other types of SSEs such as sulfide and halide SSEs show poor Li stability. Similarly, SPE can also be used to stabilize SSE/Li interfaces. With this in mind, the combination of two or more types of SSEs may be a promising direction to realize practical SSLBs.

### (3) Battery manufacturing

Battery manufacturing is another important consideration for high energy density SSLBs based on thin SSEs. The stacking manufacturing method is a similar approach applied in state-of-the-art liquid electrolyte-based LIBs. However, in the liquid electrolyte systems, the interface issue can be ignored due to the high ionic conductivity and good wettability of liquid electrolytes. In contrast, the assembly of individually constructed components in SSLBs will lead to serious interfacial issues. Post-treatment processes such as heating, pressing, and liquid electrolyte infusion should be investigated for practical application. Slurry casting and extrusion manufacturing processes show promising potential due to their ease of automation.<sup>58,77</sup> Nevertheless, only a few products have been produced. With this in mind, more effort should be devoted towards developing pouch cells based on these two methods. It is likely that large-scale manufacturing will be first achieved with polymer and polymer-based hybrid electrolytes due to their better mechanical properties and environmental stability. As one of the most popular methods, tape casting has been widely used in fabricating thin oxide SSEs and SSLBs. Nevertheless, the manufacturing efficiency and scalability are still insufficient compared with the aforementioned processes. In addition, more battery manufacturing methods should be explored, especially for the development of large size oxide-based SSLBs.<sup>44-46</sup>

### (4) Advanced characterization techniques

Advanced characterization techniques are helpful for understanding the underlying  $\text{Li}^+$  transport rules, reaction processes and mechanisms in SSLBs, which can provide guidance for the rational design of SSEs with high ionic conductivity and compatibility with electrodes. *In situ* characterization techniques are more informative than *ex situ* characterization techniques. With this in mind, more effort should be devoted towards developing novel characterization techniques aimed to reveal the underlying mechanisms related to anodes, cathodes, and SSEs and their interfaces. Considering the limited and incomplete information obtained from any individual characterization technique, we strongly recommend the combination of multiple *in situ* characterization techniques to

provide a more comprehensive understanding to aid in the development of high-performance SSLBs.

Generally speaking, thin SSEs are essential to realizing high energy density SSLBs. However, their development and manufacturing are still in a state of infancy and more work should be focused on both fundamental studies and engineering design to solve the many challenges.

## Conflicts of interest

The authors declare no conflicts of interest.

## Acknowledgements

This work was partly supported by the Natural Sciences and Engineering Research Council of Canada (NSERC), Canada Research Chairs Program (CRC), Canada Foundation for Innovation (CFI), Ontario Research Fund, China Automotive Battery Research Institute Co., Ltd, GLABAT Solid-State Battery Inc. and University of Western Ontario.

## References

- J.-M. Tarascon and M. Armand, *Nature*, 2001, **414**, 359–367.
- K. Xu, *Chem. Rev.*, 2004, **104**, 4303–4417.
- X. Yang, X. Li, K. Adair, H. Zhang and X. Sun, *Electrochem. Energy Rev.*, 2018, **1**, 239–293.
- X. Yang, J. Luo and X. Sun, *Chem. Soc. Rev.*, 2020, **49**, 2140–2195.
- Y. Zhao, K. Zheng and X. Sun, *Joule*, 2018, **2**, 2583–2604.
- E. Umeshbabu, B. Zheng and Y. Yang, *Electrochem. Energy Rev.*, 2019, **2**, 199–230.
- Q. Zhou, J. Ma, S. Dong, X. Li and G. Cui, *Adv. Mater.*, 2019, **31**, 1902029.
- A. Manthiram, X. Yu and S. Wang, *Nat. Rev. Mater.*, 2017, **2**, 16103.
- Z. Xue, D. He and X. Xie, *J. Mater. Chem. A*, 2015, **3**, 19218–19253.
- J. Liang, J. Luo, Q. Sun, X. Yang, R. Li and X. Sun, *Energy Storage Mater.*, 2019, **21**, 308–334.
- Q. Liu, Z. Geng, C. Han, Y. Fu, S. Li, Y.-B. He, F. Kang and B. Li, *J. Power Sources*, 2018, **389**, 120–134.
- N. Kamaya, K. Homma, Y. Yamakawa, M. Hirayama, R. Kanno, M. Yonemura, T. Kamiyama, Y. Kato, S. Hama, K. Kawamoto and A. Mitsui, *Nat. Mater.*, 2011, **10**, 682–686.
- Y. Kato, S. Hori, T. Saito, K. Suzuki, M. Hirayama, A. Mitsui, M. Yonemura, H. Iba and R. Kanno, *Nat. Energy*, 2016, **1**, 16030.
- X. Li, J. Liang, J. Luo, M. Norouzi Banis, C. Wang, W. Li, S. Deng, C. Yu, F. Zhao, Y. Hu, T.-K. Sham, L. Zhang, S. Zhao, S. Lu, H. Huang, R. Li, K. R. Adair and X. Sun, *Energy Environ. Sci.*, 2019, **12**, 2665–2671.
- X. Li, J. Liang, X. Yang, K. R. Adair, C. Wang, F. Zhao and X. Sun, *Energy Environ. Sci.*, 2020, **13**, 1429–1461.
- S. Wang, Q. Bai, A. M. Nolan, Y. Liu, S. Gong, Q. Sun and Y. Mo, *Angew. Chem., Int. Ed.*, 2019, **58**, 8039–8043.
- L. Zhou, C. Y. Kwok, A. Shyamsunder, Q. Zhang, X. Wu and L. F. Nazar, *Energy Environ. Sci.*, 2020, **13**, 2056–2063.
- X. Li, J. Liang, K. R. Adair, J. Li, W. Li, F. Zhao, Y. Hu, T. K. Sham, L. Zhang, S. Zhao, S. Lu, H. Huang, R. Li, N. Chen and X. Sun, *Nano Lett.*, 2020, **20**, 4384–4392.
- T. Asano, A. Sakai, S. Ouchi, M. Sakaida, A. Miyazaki and S. Hasegawa, *Adv. Mater.*, 2018, **30**, e1803075.
- X. Li, J. Liang, N. Chen, J. Luo, K. R. Adair, C. Wang, M. N. Banis, T. K. Sham, L. Zhang, S. Zhao, S. Lu, H. Huang, R. Li and X. Sun, *Angew. Chem., Int. Ed.*, 2019, **58**, 16427–16432.
- R. Chen, Q. Li, X. Yu, L. Chen and H. Li, *Chem. Rev.*, 2020, **120**, 6820–6877.
- J. Yi, S. Guo, P. He and H. Zhou, *Energy Environ. Sci.*, 2017, **10**, 860–884.
- Y.-G. Lee, S. Fujiki, C. Jung, N. Suzuki, N. Yashiro, R. Omoda, D.-S. Ko, T. Shiratsuchi, T. Sugimoto, S. Ryu, J. H. Ku, T. Watanabe, Y. Park, Y. Aihara, D. Im and I. T. Han, *Nat. Energy*, 2020, **5**, 299–308.
- Y. Liu, D. Lin, Y. Jin, K. Liu, X. Tao, Q. Zhang, X. Zhang and Y. Cui, *Sci. Adv.*, 2017, **3**, eaao0713.
- Q. Han, X. Li, X. Shi, H. Zhang, D. Song, F. Ding and L. Zhang, *J. Mater. Chem. A*, 2019, **7**, 3895–3902.
- H. Nagata and Y. Chikusa, *Energy Technol.*, 2016, **4**, 484–489.
- C. Wang, J. Liang, S. Hwang, X. Li, Y. Zhao, K. Adair, C. Zhao, X. Li, S. Deng, X. Lin, X. Yang, R. Li, H. Huang, L. Zhang, S. Lu, D. Su and X. Sun, *Nano Energy*, 2020, **72**, 104686.
- H. Huo, Y. Chen, R. Li, N. Zhao, J. Luo, J. G. Pereira da Silva, R. Mücke, P. Kaghazchi, X. Guo and X. Sun, *Energy Environ. Sci.*, 2020, **13**, 127–134.
- L. Liu, J. Xu, S. Wang, F. Wu, H. Li and L. Chen, *eTransportation*, 2019, **1**, 100010.
- J. Xiao, Q. Li, Y. Bi, M. Cai, B. Dunn, T. Glossmann, J. Liu, T. Osaka, R. Sugiura, B. Wu, J. Yang, J.-G. Zhang and M. S. Whittingham, *Nat. Energy*, 2020, **5**, 561–568.
- X. Yang, Q. Sun, C. Zhao, X. Gao, K. Adair, Y. Zhao, J. Luo, X. Lin, J. Liang, H. Huang, L. Zhang, S. Lu, R. Li and X. Sun, *Energy Storage Mater.*, 2019, **22**, 194–199.
- X. Yang, Q. Sun, C. Zhao, X. Gao, K. R. Adair, Y. Liu, J. Luo, X. Lin, J. Liang, H. Huang, L. Zhang, R. Yang, S. Lu, R. Li and X. Sun, *Nano Energy*, 2019, **61**, 567–575.
- X. Li, D. Wang, H. Wang, H. Yan, Z. Gong and Y. Yang, *ACS Appl. Mater. Interfaces*, 2019, **11**, 22745–22753.
- C. Ma, K. Dai, H. Hou, X. Ji, L. Chen, D. G. Ivey and W. Wei, *Adv. Sci.*, 2018, **5**, 1700996.
- X. Yan, Z. Li, H. Ying, F. Nie, L. Xue, Z. Wen and W.-Q. Han, *Ionics*, 2017, **24**, 1545–1551.
- X. Chen, W. He, L.-X. Ding, S. Wang and H. Wang, *Energy Environ. Sci.*, 2019, **12**, 938–944.
- H. Yuan, H.-X. Nan, C.-Z. Zhao, G.-L. Zhu, Y. Lu, X.-B. Cheng, Q.-B. Liu, C.-X. He, J.-Q. Huang and Q. Zhang, *Batteries Supercaps*, 2020, **3**, 596–603.
- M. Jabbari, R. Bulatova, A. I. Y. Tok, C. R. H. Bahl, E. Mitsoulis and J. H. Hattel, *Mater. Sci. Eng., B*, 2016, **212**, 39–61.

- 39 M. Zhang, Z. Huang, J. Cheng, O. Yamamoto, N. Imanishi, B. Chi, J. Pu and J. Li, *J. Alloys Compd.*, 2014, **590**, 147–152.
- 40 A. Sakuda, K. Kuratani, M. Yamamoto, M. Takahashi, T. Takeuchi and H. Kobayashi, *J. Electrochem. Soc.*, 2017, **164**, A2474–A2478.
- 41 Z. Jiang, S. Wang, X. Chen, W. Yang, X. Yao, X. Hu, Q. Han and H. Wang, *Adv. Mater.*, 2020, **32**, e1906221.
- 42 Y. Zhu, G. Chen, J. Sun, J. Wang, T. Wu, W. Dai and L. Lu, *Mater. Technol.*, 2020, 1–8, DOI: 10.1080/10667857.2020.1713452.
- 43 T. Ates, M. Keller, J. Kulisch, T. Adermann and S. Passerini, *Energy Storage Mater.*, 2019, **17**, 204–210.
- 44 K. Fu, Y. Gong, G. T. Hitz, D. W. McOwen, Y. Li, S. Xu, Y. Wen, L. Zhang, C. Wang, G. Pastel, J. Dai, B. Liu, H. Xie, Y. Yao, E. D. Wachsman and L. Hu, *Energy Environ. Sci.*, 2017, **10**, 1568–1575.
- 45 S. Xu, D. W. McOwen, L. Zhang, G. T. Hitz, C. Wang, Z. Ma, C. Chen, W. Luo, J. Dai, Y. Kuang, E. M. Hitz, K. Fu, Y. Gong, E. D. Wachsman and L. Hu, *Energy Storage Mater.*, 2018, **15**, 458–464.
- 46 G. T. Hitz, D. W. McOwen, L. Zhang, Z. Ma, Z. Fu, Y. Wen, Y. Gong, J. Dai, T. R. Hamann, L. Hu and E. D. Wachsman, *Mater. Today*, 2019, **22**, 50–57.
- 47 K. K. Fu, Y. Gong, J. Dai, A. Gong, X. Han, Y. Yao, C. Wang, Y. Wang, Y. Chen, C. Yan, Y. Li, E. D. Wachsman and L. Hu, *Proc. Natl. Acad. Sci. U. S. A.*, 2016, **113**, 7094–7099.
- 48 J. Wan, J. Xie, X. Kong, Z. Liu, K. Liu, F. Shi, A. Pei, H. Chen, W. Chen, J. Chen, X. Zhang, L. Zong, J. Wang, L. Q. Chen, J. Qin and Y. Cui, *Nat. Nanotechnol.*, 2019, **14**, 705–711.
- 49 J. Bae, Y. Li, J. Zhang, X. Zhou, F. Zhao, Y. Shi, J. B. Goodenough and G. Yu, *Angew. Chem., Int. Ed.*, 2018, **57**, 2096–2100.
- 50 D. H. Kim, Y.-H. Lee, Y. B. Song, H. Kwak, S.-Y. Lee and Y. S. Jung, *ACS Energy Lett.*, 2020, **5**, 718–727.
- 51 J. Dai, K. Fu, Y. Gong, J. Song, C. Chen, Y. Yao, G. Pastel, L. Zhang, E. Wachsman and L. Hu, *ACS Mater. Lett.*, 2019, **1**, 354–361.
- 52 H. Zhai, P. Xu, M. Ning, Q. Cheng, J. Mandal and Y. Yang, *Nano Lett.*, 2017, **17**, 3182–3187.
- 53 Y. J. Nam, S. J. Cho, D. Y. Oh, J. M. Lim, S. Y. Kim, J. H. Song, Y. G. Lee, S. Y. Lee and Y. S. Jung, *Nano Lett.*, 2015, **15**, 3317–3323.
- 54 R. Xu, J. Yue, S. Liu, J. Tu, F. Han, P. Liu and C. Wang, *ACS Energy Lett.*, 2019, **4**, 1073–1079.
- 55 J. M. Whiteley, P. Taynton, W. Zhang and S.-H. Lee, *Adv. Mater.*, 2015, **27**, 6922–6927.
- 56 P. C. Howlett, F. Ponzio, J. Fang, T. Lin, L. Jin, N. Iranipour and J. Efthimiadis, *Phys. Chem. Chem. Phys.*, 2013, **15**, 13784–13789.
- 57 M. Li, J. E. Frerichs, M. Kolek, W. Sun, D. Zhou, C. J. Huang, B. J. Hwang, M. R. Hansen, M. Winter and P. Bieker, *Adv. Funct. Mater.*, 2020, **30**, 1910123.
- 58 J. Schnell, T. Günther, T. Knoche, C. Vieider, L. Köhler, A. Just, M. Keller, S. Passerini and G. Reinhart, *J. Power Sources*, 2018, **382**, 160–175.
- 59 H. Xie, Y. Bao, J. Cheng, C. Wang, E. M. Hitz, C. Yang, Z. Liang, Y. Zhou, S. He, T. Li and L. Hu, *ACS Energy Lett.*, 2019, **4**, 2668–2674.
- 60 H. Wang, Z. D. Hood, Y. Xia and C. Liang, *J. Mater. Chem. A*, 2016, **4**, 8091–8096.
- 61 R. Chen, W. Qu, X. Guo, L. Li and F. Wu, *Mater. Horiz.*, 2016, **3**, 487–516.
- 62 M. Keller, G. B. Appetecchi, G.-T. Kim, V. Sharova, M. Schneider, J. Schuhmacher, A. Roters and S. Passerini, *J. Power Sources*, 2017, **353**, 287–297.
- 63 G. B. Appetecchi, J. H. Shin, F. Alessandrini and S. Passerini, *J. Power Sources*, 2005, **143**, 236–242.
- 64 C. Bae, R. Rao and E. Shradler, EP2966708B1, 2018.
- 65 M. P. Browne, E. Redondo and M. Pumera, *Chem. Rev.*, 2020, **120**, 2783–2810.
- 66 X. Gao, Q. Sun, X. Yang, J. Liang, A. Koo, W. Li, J. Liang, J. Wang, R. Li, F. B. Holness, A. D. Price, S. Yang, T.-K. Sham and X. Sun, *Nano Energy*, 2019, **56**, 595–603.
- 67 D. W. McOwen, S. Xu, Y. Gong, Y. Wen, G. L. Godbey, J. E. Gritton, T. R. Hamann, J. Dai, G. T. Hitz, L. Hu and E. D. Wachsman, *Adv. Mater.*, 2018, **30**, e1707132.
- 68 S. H. Kim, J. H. Kim, S. J. Cho and S. Y. Lee, *Adv. Energy Mater.*, 2019, **9**, 1901841.
- 69 C. Peng, Y. Kamiike, Y. Liang, K. Kuroda and M. Okido, *ACS Sustainable Chem. Eng.*, 2019, **7**, 10751–10762.
- 70 S. P. Woo, N. Kakati, I. Y. Kim, S. H. Lee and Y. S. Yoon, *J. Korean Phys. Soc.*, 2016, **69**, 617–622.
- 71 Z. D. Hood, H. Wang, A. S. Pandian, R. Peng, K. D. Gilroy, M. Chi, C. Liang and Y. Xia, *Adv. Energy Mater.*, 2018, **8**, 1800014.
- 72 H. Duan, Y. X. Yin, Y. Shi, P. F. Wang, X. D. Zhang, C. P. Yang, J. L. Shi, R. Wen, Y. G. Guo and L. J. Wan, *J. Am. Chem. Soc.*, 2018, **140**, 82–85.
- 73 Q. Zhao, X. Liu, S. Stalin, K. Khan and L. A. Archer, *Nat. Energy*, 2019, **4**, 365–373.
- 74 S. Ito, M. Nakakita, Y. Aihara, T. Uehara and N. Machida, *J. Power Sources*, 2014, **271**, 342–345.
- 75 Y. Wang, D. Lu, M. Bowden, P. Z. El Khoury, K. S. Han, Z. D. Deng, J. Xiao, J.-G. Zhang and J. Liu, *Chem. Mater.*, 2018, **30**, 990–997.
- 76 F. Han, J. Yue, X. Fan, T. Gao, C. Luo, Z. Ma, L. Suo and C. Wang, *Nano Lett.*, 2016, **16**, 4521–4527.
- 77 D. H. S. Tan, A. Banerjee, Z. Chen and Y. S. Meng, *Nat. Nanotechnol.*, 2020, **15**, 170–180.
- 78 P.-A. Lavoie, R. Laliberte, J. Dube and Y. Gagnon, EP1568090B1, 2004.
- 79 C. L. Cobb and C.-J. Bae, US9590232B2, 2017.
- 80 G. Zhong, C. Wang, R. Wang, W. Ping, S. Xu, H. Qiao, M. Cui, X. Wang, Y. Zhou, D. J. Kline, M. R. Zachariah and L. Hu, *Energy Storage Mater.*, 2020, **30**, 385–391.
- 81 F. Han, J. Yue, C. Chen, N. Zhao, X. Fan, Z. Ma, T. Gao, F. Wang, X. Guo and C. Wang, *Joule*, 2018, **2**, 497–508.
- 82 D. Lin, P. Y. Yuen, Y. Liu, W. Liu, N. Liu, R. H. Dauskardt and Y. Cui, *Adv. Mater.*, 2018, **30**, e1802661.
- 83 H. Duan, Y.-X. Yin, X.-X. Zeng, J.-Y. Li, J.-L. Shi, Y. Shi, R. Wen, Y.-G. Guo and L.-J. Wan, *Energy Storage Mater.*, 2018, **10**, 85–91.

- 84 K. Gao, M. He, Y. Li, Y. Zhang, J. Gao, X. Li, Z. Cui, Z. Zhan and T. Zhang, *J. Alloys Compd.*, 2019, **791**, 923–928.
- 85 K. Zhu, Y. Liu and J. Liu, *RSC Adv.*, 2014, **4**, 42278–42284.
- 86 T.-J. Cai, Y.-H. Lo and J.-J. Wu, *Mater. Today Energy*, 2019, **13**, 119–124.
- 87 J. Wu, Z. Rao, Z. Cheng, L. Yuan, Z. Li and Y. Huang, *Adv. Energy Mater.*, 2019, **9**, 1902767.
- 88 X. Yang, M. Jiang, X. Gao, D. Bao, Q. Sun, N. Holmes, H. Duan, S. Mukherjee, K. Adair, C. Zhao, J. Liang, W. Li, J. Li, Y. Liu, H. Huang, L. Zhang, S. Lu, Q. Lu, R. Li, C. V. Singh and X. Sun, *Energy Environ. Sci.*, 2020, **13**, 1318–1325.
- 89 Y. Zhu, X. He and Y. Mo, *ACS Appl. Mater. Interfaces*, 2015, **7**, 23685–23693.
- 90 H. Duan, M. Fan, W. P. Chen, J. Y. Li, P. F. Wang, W. P. Wang, J. L. Shi, Y. X. Yin, L. J. Wan and Y. G. Guo, *Adv. Mater.*, 2019, **31**, 1807789.
- 91 C. Wang, T. Wang, L. Wang, Z. Hu, Z. Cui, J. Li, S. Dong, X. Zhou and G. Cui, *Adv. Sci.*, 2019, **6**, 1901036.
- 92 H. Shen, E. Yi, M. Amores, L. Cheng, N. Tamura, D. Y. Parkinson, G. Chen, K. Chen and M. Doeff, *J. Mater. Chem. A*, 2019, **7**, 20861–20870.
- 93 M. Yamamoto, Y. Terauchi, A. Sakuda and M. Takahashi, *Sci. Rep.*, 2018, **8**, 1212.
- 94 C. Wang, X. Li, Y. Zhao, M. N. Banis, J. Liang, X. Li, Y. Sun, K. R. Adair, Q. Sun, Y. Liu, F. Zhao, S. Deng, X. Lin, R. Li, Y. Hu, T. K. Sham, H. Huang, L. Zhang, R. Yang, S. Lu and X. Sun, *Small Methods*, 2019, **3**, 1900261.
- 95 E. Umeshbabu, B. Zheng and Y. Yang, *Electrochem. Energy Rev.*, 2019, **2**, 199–230.
- 96 X. Tao, Y. Liu, W. Liu, G. Zhou, J. Zhao, D. Lin, C. Zu, O. Sheng, W. Zhang, H. W. Lee and Y. Cui, *Nano Lett.*, 2017, **17**, 2967–2972.
- 97 X. Judez, H. Zhang, C. Li, J. A. Gonzalez-Marcos, Z. Zhou, M. Armand and L. M. Rodriguez-Martinez, *J. Phys. Chem. Lett.*, 2017, **8**, 1956–1960.
- 98 G. G. Eshetu, X. Judez, C. Li, O. Bondarchuk, L. M. Rodriguez-Martinez, H. Zhang and M. Armand, *Angew. Chem., Int. Ed.*, 2017, **56**, 15368–15372.
- 99 Y. Gong, K. Fu, S. Xu, J. Dai, T. R. Hamann, L. Zhang, G. T. Hitz, Z. Fu, Z. Ma, D. W. McOwen, X. Han, L. Hu and E. D. Wachsman, *Mater. Today*, 2018, **21**, 594–601.
- 100 H. T. T. Le, D. T. Ngo, P. N. Didwal, J. G. Fisher, C.-N. Park, I.-D. Kim and C.-J. Park, *J. Mater. Chem. A*, 2019, **7**, 3150–3160.
- 101 X. Zhu, T. Zhao, P. Tan, Z. Wei and M. Wu, *Nano Energy*, 2016, **26**, 565–576.
- 102 X. B. Zhu, T. S. Zhao, Z. H. Wei, P. Tan and G. Zhao, *Energy Environ. Sci.*, 2015, **8**, 2782–2790.
- 103 M. Balaish, E. Peled, D. Golodnitsky and Y. Ein-Eli, *Angew. Chem., Int. Ed.*, 2015, **127**, 446–450.
- 104 N. Bonnet-Mercier, R. A. Wong, M. L. Thomas, A. Dutta, K. Yamanaka, C. Yogi, T. Ohta and H. R. Byon, *Sci. Rep.*, 2014, **4**, 7127.
- 105 G. A. Elia and J. Hassoun, *Sci. Rep.*, 2015, **5**, 12307.
- 106 P. Hovington, M. Lagace, A. Guerfi, P. Bouchard, A. Mauger, C. M. Julien, M. Armand and K. Zaghib, *Nano Lett.*, 2015, **15**, 2671–2678.
- 107 Y. J. Nam, D. Y. Oh, S. H. Jung and Y. S. Jung, *J. Power Sources*, 2018, **375**, 93–101.
- 108 Y. Xiao, Y. Wang, S.-H. Bo, J. C. Kim, L. J. Miara and G. Ceder, *Nat. Rev. Mater.*, 2019, **5**, 105–126.
- 109 A. Banerjee, X. Wang, C. Fang, E. A. Wu and Y. S. Meng, *Chem. Rev.*, 2020, **120**, 6878–6933.
- 110 K. Nie, X. Wang, J. Qiu, Y. Wang, Q. Yang, J. Xu, X. Yu, H. Li, X. Huang and L. Chen, *ACS Energy Lett.*, 2020, **5**, 826–832.
- 111 Y. Xiang, X. Li, Y. Cheng, X. Sun and Y. Yang, *Mater. Today*, 2020, **36**, 139–157.
- 112 S. Lou, Z. Yu, Q. Liu, H. Wang, M. Chen and J. Wang, *Chemistry*, 2020, **6**, 2199–2218.
- 113 L. Cheng, W. Chen, M. Kunz, K. Persson, N. Tamura, G. Chen and M. Doeff, *ACS Appl. Mater. Interfaces*, 2015, **7**, 2073–2081.
- 114 C. Vinod Chandran, S. Pristat, E. Witt, F. Tietz and P. Heitjans, *J. Phys. Chem. C*, 2016, **120**, 8436–8442.
- 115 S. Harm, A.-K. Hatz, I. Moudrakovski, R. Eger, A. Kuhn, C. Hoch and B. V. Lotsch, *Chem. Mater.*, 2019, **31**, 1280–1288.
- 116 S. Ganapathy, C. Yu, E. R. H. van Eck and M. Wagemaker, *ACS Energy Lett.*, 2019, **4**, 1092–1097.
- 117 D. Safanama, N. Sharma, R. P. Rao, H. E. A. Brand and S. Adams, *J. Mater. Chem. A*, 2016, **4**, 7718–7726.
- 118 A. A. Hubaud, D. J. Schroeder, B. J. Ingram, J. S. Okasinski and J. T. Vaughey, *J. Alloys Compd.*, 2015, **644**, 804–807.
- 119 H. Stöffler, T. Zinkevich, M. Yavuz, A. Senyshyn, J. Kulisch, P. Hartmann, T. Adermann, S. Randau, F. H. Richter, J. Janek, S. Indris and H. Ehrenberg, *J. Phys. Chem. C*, 2018, **122**, 15954–15965.
- 120 W. Li, J. Liang, M. Li, K. R. Adair, X. Li, Y. Hu, Q. Xiao, R. Feng, R. Li, L. Zhang, S. Lu, H. Huang, S. Zhao, T.-K. Sham and X. Sun, *Chem. Mater.*, 2020, **32**, 7019–7027.
- 121 Y. Chen, E. Rangasamy, C. R. dela Cruz, C. Liang and K. An, *J. Mater. Chem. A*, 2015, **3**, 22868–22876.
- 122 <https://neutrons.ornl.gov/content/neutrons-offer-guide-getting-more-out-solid-state-lithium-ion-batteries>.
- 123 Y. Chen, E. Rangasamy, C. Liang and K. An, *Chem. Mater.*, 2015, **27**, 5491–5494.
- 124 M. B. Dixit, M. Regala, F. Shen, X. Xiao and K. B. Hatzell, *ACS Appl. Mater. Interfaces*, 2019, **11**, 2022–2030.
- 125 F. Shen, M. B. Dixit, X. Xiao and K. B. Hatzell, *ACS Energy Lett.*, 2018, **3**, 1056–1061.
- 126 X. Ke, Y. Wang, G. Ren and C. Yuan, *Energy Storage Mater.*, 2020, **26**, 313–324.
- 127 H.-Y. Li, B. Huang, Z. Huang and C.-A. Wang, *Ceram. Int.*, 2019, **45**, 18115–18118.
- 128 F. Shen, W. Guo, D. Zeng, Z. Sun, J. Gao, J. Li, B. Zhao, B. He and X. Han, *ACS Appl. Mater. Interfaces*, 2020, **12**, 30313–30319.
- 129 N. Seitzman, H. Guthrey, D. B. Sulas, H. A. S. Platt, M. Al-Jassim and S. Pylypenko, *J. Electrochem. Soc.*, 2018, **165**, A3732–A3737.
- 130 J. Tippens, J. C. Miers, A. Afshar, J. A. Lewis, F. J. Q. Cortes, H. Qiao, T. S. Marchese, C. V. Di Leo, C. Saldana and M. T. McDowell, *ACS Energy Lett.*, 2019, **4**, 1475–1483.

- 131 E. Kazyak, R. Garcia-Mendez, W. S. LePage, A. Sharafi, A. L. Davis, A. J. Sanchez, K.-H. Chen, C. Haslam, J. Sakamoto and N. P. Dasgupta, *Matter*, 2020, **2**, 1025–1048.
- 132 C. Ma, Y. Cheng, K. Yin, J. Luo, A. Sharafi, J. Sakamoto, J. Li, K. L. More, N. J. Dudley and M. Chi, *Nano Lett.*, 2016, **16**, 7030–7036.
- 133 P. H. Chien, X. Feng, M. Tang, J. T. Rosenberg, S. O'Neill, J. Zheng, S. C. Grant and Y. Y. Hu, *J. Phys. Chem. Lett.*, 2018, **9**, 1990–1998.
- 134 S. Wenzel, S. Randau, T. Leichtweiß, D. A. Weber, J. Sann, W. G. Zeier and J. R. Janek, *Chem. Mater.*, 2016, **28**, 2400–2407.
- 135 S. Wenzel, T. Leichtweiss, D. Krüger, J. Sann and J. Janek, *Solid State Ionics*, 2015, **278**, 98–105.
- 136 K. N. Wood, K. X. Steirer, S. E. Hafner, C. Ban, S. Santhanagopalan, S.-H. Lee and G. Teeter, *Nat. Commun.*, 2018, **9**, 2490.
- 137 F. Hippauf, B. Schumm, S. Doerfler, H. Althues, S. Fujiki, T. Shiratsuchi, T. Tsujimura, Y. Aihara and S. Kaskel, *Energy Storage Mater.*, 2019, **21**, 390–398.
- 138 W. Zhang, D. Schröder, T. Arlt, I. Manke, R. Koerver, R. Pinedo, D. A. Weber, J. Sann, W. G. Zeier and J. Janek, *J. Mater. Chem. A*, 2017, **5**, 9929–9936.
- 139 W. J. Li, M. Hirayama, K. Suzuki and R. Kanno, *Mater. Trans.*, 2016, **57**, 549–552.
- 140 R. Koerver, W. Zhang, L. de Biasi, S. Schweidler, A. O. Kondrakov, S. Kolling, T. Brezesinski, P. Hartmann, W. G. Zeier and J. Janek, *Energy Environ. Sci.*, 2018, **11**, 2142–2158.
- 141 X. Gao, X. Yang, Q. Sun, J. Luo, J. Liang, W. Li, J. Wang, S. Wang, M. Li, R. Li, T.-K. Sham and X. Sun, *Energy Storage Mater.*, 2020, **24**, 682–688.
- 142 H. Chen, A. Pei, J. Wan, D. Lin, R. Vilá, H. Wang, D. Mackanic, H.-G. Steinrück, W. Huang, Y. Li, A. Yang, J. Xie, Y. Wu, H. Wang and Y. Cui, *Joule*, 2020, **4**, 938–952.
- 143 X. Gao, X. Yang, K. Adair, X. Li, J. Liang, Q. Sun, Y. Zhao, R. Li, T. K. Sham and X. Sun, *Adv. Energy Mater.*, 2020, **10**, 1903753.
- 144 X. Gao, X. Yang, K. Adair, J. Liang, Q. Sun, Y. Zhao, R. Li, T. K. Sham and X. Sun, *Adv. Funct. Mater.*, 2020, 2005357, DOI: 10.1002/adfm.202005357.
- 145 D. Cao, X. Sun, Q. Li, A. Natan, P. Xiang and H. Zhu, *Matter*, 2020, **3**, 57–94.
- 146 X. Yang, X. Gao, S. Mukherjee, K. Doyle-Davis, J. Fu, W. Li, Q. Sun, F. Zhao, M. Jiang, Y. Hu, H. Huang, L. Zhang, S. Lu, R. Li, T. K. Sham, C. V. Singh and X. Sun, *Adv. Energy Mater.*, 2020, **10**, 2001191.
- 147 Y. Su, L. Ye, W. Fitzhugh, Y. Wang, E. Gil-González, I. Kim and X. Li, *Energy Environ. Sci.*, 2020, **13**, 908–916.
- 148 X. Liang, Q. Pang, I. R. Kochetkov, M. S. Sempere, H. Huang, X. Sun and L. F. Nazar, *Nat. Energy*, 2017, **2**, 17119.
- 149 M. J. Wang, E. Carmona, A. Gupta, P. Albertus and J. Sakamoto, *Nat. Commun.*, 2020, **11**, 5201.
- 150 F. Han, A. S. Westover, J. Yue, X. Fan, F. Wang, M. Chi, D. N. Leonard, N. J. Dudley, H. Wang and C. Wang, *Nat. Energy*, 2019, **4**, 187–196.
- 151 Y. Liu, Q. Sun, Y. Zhao, B. Wang, P. Kaghazchi, K. R. Adair, R. Li, C. Zhang, J. Liu, L. Y. Kuo, Y. Hu, T. K. Sham, L. Zhang, R. Yang, S. Lu, X. Song and X. Sun, *ACS Appl. Mater. Interfaces*, 2018, **10**, 31240–31248.
- 152 J. Liang, Q. Sun, Y. Zhao, Y. Sun, C. Wang, W. Li, M. Li, D. Wang, X. Li, Y. Liu, K. Adair, R. Li, L. Zhang, R. Yang, S. Lu, H. Huang and X. Sun, *J. Mater. Chem. A*, 2018, **6**, 23712–23719.
- 153 R. Sheil and J. P. Chang, *J. Vac. Sci. Technol., A*, 2020, **38**, 032411.
- 154 C. Hu, Y. Shen, M. Shen, X. Liu, H. Chen, C. Liu, T. Kang, F. Jin, L. Li, J. Li, Y. Li, N. Zhao, X. Guo, W. Lu, B. Hu and L. Chen, *J. Am. Chem. Soc.*, 2020, **142**, 18035–18041.
- 155 S. Deng, X. Li, Z. Ren, W. Li, J. Luo, J. Liang, J. Liang, M. N. Banis, M. Li, Y. Zhao, X. Li, C. Wang, Y. Sun, Q. Sun, R. Li, Y. Hu, H. Huang, L. Zhang, S. Lu, J. Luo and X. Sun, *Energy Storage Mater.*, 2020, **27**, 117–123.